T.R.
SAKARYA UNIVERSITY
INSTITUTE OF NATURAL SCIENCE

SIMULATION OF A TOROIDAL GANTRY FOR PROTON THERAPY BY FLUKA

PhD THESIS

Mosleh Ali MOHAMMAD

Physics Department

JULY 2024

T.R.
SAKARYA UNIVERSITY
INSTITUTE OF NATURAL SCIENCE

SIMULATION OF A TOROIDAL GANTRY FOR PROTON THERAPY BY FLUKA

PhD THESIS

Mosleh Ali MOHAMMAD

Physıcs Department

Thesis Advisor: Prof. Dr. Mehmet BEKTAŞOĞLU

JULY 2024

The thesis work titled "SIMULATION OF A TOROIDAL GANTRY FOR PROTON THERAPY BY FLUKA," prepared by Mosleh Ali Mohammad, was accepted by the following jury on 25/07/2024 by unanimously/majority of votes as a PhD THESIS in Sakarya University Institute of Natural Sciences, Department of Physics.

Thesis Jury

Head of Jury :   **Prof. Dr. Mehmet BEKTAŞOĞLU** (Advisor)   ....
Sakarya University

Jury Member :   **Prof. Dr. Kudret YILDIRIM**   ....
Sakarya University

Jury Member :   **Assoc. Prof. Ali Serdar ARIKAN**   ....
Sakarya University

Jury Member :   **Assoc. Prof. Halil ARSLAN**   ....
Sakarya University of Applied Sciences

Jury Member :   **Asst. Prof. Yakup BORAN**   ....
Sakarya University of Applied Sciences

STATEMENT OF COMPLIANCE WITH THE ETHICAL PRINCIPLES AND RULES

I declare that the thesis work titled " SIMULATION OF A TOROIDAL GANTRY FOR PROTON THERAPY BY FLUKA", which I have prepared in accordance with Sakarya University Graduate School of Natural and Applied Sciences regulations and Higher Education Institutions Scientific Research and Publication Ethics Directive, belongs to me, is an original work, I have acted in accordance with the regulations and directives mentioned above at all stages of my study, I did not get the innovations and results contained in the thesis from anywhere else, I duly cited the references for the works I used in my thesis, I did not submit this thesis to another scientific committee for academic purposes and to obtain a title, in accordance with the articles 9/2 and 22/2 of the Sakarya University Graduate Education and Training Regulation published in the Official Gazette dated 20.04.2016, a report was received in accordance with the criteria determined by the graduate school using the plagiarism software program to which Sakarya University is a subscriber, I accept all kinds of legal responsibility that may arise in case of a situation contrary to this statement.

(24/06/2024)

Mosleh Ali MOHAMMAD

To my wife and daughter

ACKNOWLEDGMENTS

TABLE OF CONTENTS

ABBREVIATIONS

A	: Atomic Mass
B	: Boron
BNCT	: Boron neutron capture therapy
CERN	: European Council for Nuclear Research
CNAO	: National Centre for Oncological Hadrontherapy
d	: Deuteron
e$^-$	: Electron
e$^+$	: Positron
eV	: Electronvolts
Flair	: FLUKA Advanced Interface
FLUKA	: FLUktuierende KAskade
FNT	: Fast Neutron Therapy
Gy	: Gray
H	: Hydrogen
HIMAC	: Heavy Ion Medical Accelerator in Chiba
HIT	: Heidelberg Ion Beam Therapy Center
HITRIplus	: Heavy Ion Therapy Research Integration plus
IMPT	: Intensity Modulated Proton Therapy
IMRT	: Intensity Modulated Radiation Therapy
LET	: Linear Energy Transfer
LET$_d$	: Dose-Averaged Linear Energy Transfer
LET$_t$	: Track-Averaged Linear Energy Transfer
LINAC	: Linear Accelerator
LWFA	: Laser Wakefield Acceleration
MC	: Monte Carlo
MeV	: Mega electronvolt
n	: Neutron
N$_A$	: Avogadro's number
NASA	: National Aeronautics and Space Administration
NCT	: Neutron Capture Therapy

N_e	:	Electron density
p	:	Proton
PET	:	Positron Emission Tomography
PSI	:	Paul Scherrer Institute
PSPT	:	Passively Scattered Proton Therapy
PT	:	Particle Therapy
PTCOG	:	Particle Therapy Co-Operative Group
PWFA	:	Particle WakeField Acceleration
RBE	:	Relative Biological Effectiveness
RMSE	:	Root Mean Square Error
RT	:	Radiation Therapy
S	:	Stopping power
SOBP	:	Spread-Out Bragg Peak
UV	:	Ultraviolet
Z	:	Atomic number

SYMBOLS

h	: Planck Constant [kg m/s]
c	: Speed of Light [m/s]
λ	: Wavelength [m]
E_{γ}	: Energy of Incident Photon [MeV]
E_{b}	: Binding Energy of Electron [MeV]
ρ	: Density [kg/m^3]
m	: Mass [kg]
μ	: Total Linear Attenuation Coefficient [m^{-1}]
μ_{m}	: Mass Attenuation Coefficient [m^2/kg]
τ	: Photoelectric Cross-Section [m^{-1}]
ν	: Frequency [Hz]
σ	: Compton Cross-Section [m^{-1}]
κ	: Pair Production Coefficient [m^{-1}]
J_{en}	: Engineering current density [A/mm^2]

LIST OF TABLES

LIST OF FIGURES

SIMULATION OF A TOROIDAL GANTRY FOR PROTON THERAPY BY FLUKA

SUMMARY

Proton therapy, a rapidly evolving cancer treatment, utilizes high-energy protons to precisely target tumors. This approach minimizes damage to healthy tissue compared to conventional x-ray therapy due to the Bragg Peak phenomenon, where protons deposit most of their energy at a specific depth. This research investigates a novel design for a proton therapy gantry using FLUKA, a powerful software program for simulating particle transport.

The study begins by providing a foundational understanding of hadron therapy, encompassing the treatment process, accelerator types, and the beam delivery systems involved. Following this introduction, it delves into the core principles of radiation physics relevant to proton therapy. This includes understanding how photons and charged particles interact with matter, how stopping power influences beam penetration, how dose is calculated to determine treatment effectiveness, and the significance of the Bragg Peak for targeted therapy.

The core of the research focuses on simulating a toroidal gantry design for proton therapy using FLUKA. This distinctive gantry design employs a donut-shaped magnetic field to steer the proton beam. The simulation process involves constructions of a detailed geometrical model of the treatment setup, including the toroidal gantry, patient, etc., within FLUKA. Furthermore, the specific parameters of the proton beam, such as energy, initial direction, and intensity, are defined. A critical aspect of the work is the method developed to calculate the multipolar moments of the toroidal magnetic field, which is then integrated into the simulation tool to assess the field's impact on the proton beam.

The analysis of the simulation results encompasses several key aspects. First, the calculated magnetic field is compared to the designed field to ensure its accuracy and stability, which are critical for precise beam control. Second, the simulation evaluates how the magnetic field deflects the proton beam and how launch angles need to be adjusted to ensure the beam converges at the precise location within the patient targeted for treatment (isocenter). Furthermore, the simulation calculates the distribution of the deposited dose within the patient and analyzes the LET (Linear Energy Transfer), which describes the amount of energy deposited by the protons per unit track length. This information is crucial for understanding the biological effects of radiation on tumor cells. Finally, the simulation assesses the overall performance of the toroidal gantry design by evaluating factors like energy deposition patterns within the tumor and surrounding tissues. This analysis helps determine the accuracy of beam targeting and the potential for achieving highly conformal dose delivery, minimizing damage to healthy tissue.

In conclusion, this research utilized FLUKA software to simulate a novel toroidal gantry design for proton therapy. The study explored the fundamental principles of hadron therapy and radiation physics and analyzed the magnetic field, proton beam deflection, dose distribution, and treatment accuracy within the simulated toroidal gantry. The findings from this research can pave the way for further development and exploration of this innovative design for improved precision and effectiveness in proton therapy. Future research directions could involve exploring the potential clinical applications of the toroidal gantry design and conducting further investigations to optimize its performance for enhanced patient outcomes.

PROTON TERAPİDE KULLANILACAK TOROİDAL GENTRİNİN FLUKA İLE BENZETİMİ

ÖZET

Radyasyon, uzayda veya madde içerisinde elektromanyetik dalga veya parçacık olarak enerji yayımı veya aktarımıdır. Radyasyon, enerjisine bağlı olarak iyonizan ve iyonizan olmayan olmak üzere iki ana kategoriye ayrılır. Günümüzde radyasyon tıp, endüstri, tarım ve elektrik üretimi gibi birçok alanda insanlığın hizmetindedir.

İyonizan radyasyonun kanser tedavisinden kullanılması radyoterapi olarak isimlendirilir. Geleneksel radyoterepide yüksek enerjili fotonlardan yararlanılırken, günümüzde fotonların kullanıldığı terapinin yanı sıra proton ve karbon iyonları gibi yüklü parçacıklar aracılığıyla tümörlü hücrelerin ortadan kaldırılması uygulamaları artmaktadır. Genel olarak hadron terapi adı verilen bu tedavi yönteminde demet olarak proton kullanılması halinde uygulama proton terapi olarak isimlendirilir. Öte yandan, bu tür terapide kullanılan sistemler geleneksel radyoterapikilerle karşılaştırıldığında daha karmaşık, büyük ve pahalı olabilmekte, bu da böyle sistemlerin her merkezde kullanılabilme olanağını ortadan kaldırmaktadır.

Hadron terapide hadronların karakteristik derin-doz dağılımlarından faydalınılır. Yüksek enerjili fotonların kullanıldığı geleneksel radyoterapide fotonlar maddeyle etkileşim mekanizmaları sebebiyle tümörlü dokuların yanı sıra sağlıklı dokulara da zarar verebilirler. Hadronlar ise madde içerisinde ilerlerken ortama az miktarda enerji aktarımı yaparlar. Bu parçacıkların madde içindeki yolculukları sona ermek üzere iken ortama enerji aktarımı maksimum düzeye çıkar ve bu da madde içerisindeki derinliğe bağlı hadron enerji depolanması eğrisinde *Bragg piki* adı verilen bir tepe oluşturur. Bu kesin enerji depolanması sürecinde tümörlü hedef dokulara aktarılan enerji en üst düzeydeyken çevredeki dokulara verilen zarar en az mertebede olur.

Hadron terapinin kanser tedavisinde kullanımının yukarıda bahsedilen üstünlüklerine rağmen bazı dezavantajları mevcuttur. Bunların arasında tedavi merkezlerindeki hadron hızlandırıcı ünitesi ile hadronların hedefe yönlendirilmesi ve hedefin çeşitli yönlerden bombardıman edilmesi için kullanılan sistemlerin (*gentri*) geleneksel radyoterapidekilere kıyasla çok daha büyük, karmaşık, ağır ve pahalı olması sayılabilir. Bu tür sebeplerden dolayı dünya genelinde hadron terapiden yararlanarak kanser tedavisi uygulayan merkezlerin sayısı geleneksel radyoterapi kullanan merkezlerin sayısına göre oldukça azdır. Proton terapi merkezleri ile karbon gibi ağır iyon kullanan merkezler karşılaştırıldığında ise proton terapi merkezlerinin sayısının çok daha fazla olduğu söylenebilir.

Proton terapide kullanılan gentriler ağır iyon demetleri için kullanılanlarla karşılaştırıldığında daha küçük hacimli ve hafiftirler. Ancak yine de çapları metrelerce ve kütleleri 100 tonun üzerinde olabilmektedir. Bu gentrilerin boyutlarının küçültülmesi ve/veya kütlelerinin azaltılması yukarıda bahsedilen bir takım olumsuzlukların ortadan kaldırılmasına olanak sağlayacağı açıktır. Bu amaçla mevcut gentrilere alternatifler geliştilmeye çalışılmaktadır. Bunlardan bir tanesi de

süperiletkenler aracılığıyla daha küçük ebat ve kütleye sahip olacak şekilde tasarlanmış GaToroid adı verilen gentridir. Bu sistem büyüklük, kütle ve fiyat açısından muadillerine göre avantajlı olmanın yanı sıra sabit yapısı aracılığıyla hastayı döndürmeden hedefi farklı açılardan bombardıman etme olanağı sağlayacak şekilde planlanmıştır.

Toroidal tasarım ile birlikte süperiletken teknolojinin kullanılması hadron terapide kullanılan gentrilerin büyüklük ve kütle açısından giderek daha avantajlı hale gelmesini sağlar. Bunlara örnek olarak GaToroid adı verilen yeni geliştirilmiş bir gentri verilebilir. GaToroid kütle ve fiyat açısından muadillerine göre avantajlı olmanın yanı sıra sabit yapısı aracılığıyla karmaşık döndürme mekanizmalarına veya hastayı döndürmeye gerek kalmadan hedefin farklı açılardan bombardıman edilmesine olanak sağlayacak şekilde planlanmıştır.

Toroidal mıknatıslarla çevrelenmiş bir merkez içine GaToroid ekseni boyunca yerleştirilmiş bir hasta, farklı yönlerden ve farklı enerjilerle gelen yüklü parçacıklar tarafından bombardıman edilir ve bunların değişken manyetik alan aracılığıyla hedef bölgeye odaklanmaları sağlanır.

Bu tez çalışmasında yukarıda bahsi edilen yeni tür gentry GaToroid, bir Monte Carlo benzetim programı olan FLUKA ile incelenmiştir. Tezdeki akış ana hatlarıyla aşağıda verilmektedir.

Tezin ilk bölümünde foton, yüklü parçacıklar ve nötron gibi radyasyon çeşitlerinin maddeyle etkileşim türleri özetlenmiş, durdurma gücü (*stopping power*), menzil (*range*), lineer enerji transferi (LET) gibi terimler hakkında genel terorik bilgi verilmiştir.

İkinci bölüm hadron terapide kullanılan hızlandırıcı çeşitleri ve demet kontrol sistemleri ile çalışmasının konusunu oluşturan GaToroid isimli gentri konusunda bilgi içermektedir.

Üçüncü bölüme toroidal koordinatlardan bahsedilerek giriş yapılmıştır. Bu çalışmadaki temel amaçlardan biri farklı enerjilere sahip protonların GaToroid içinde saptırılarak tümörlü bölgeyi temsil eden bir noktaya odaklandırılmasının sağlanmasıdır. Bunun için gentri içinde enerjileri farklı protonların farklı şekilde sapmasına olanak sağlayacak sabit olmayan bir manyetik alana ihtiyaç duyulur. Bu bölümün geri kalan kısmında yukarıda sözü edilen türdeki bir manyetik alan bilgisine ulaşmak amacıyla kullanılan teknik özetlenmiştir.

Tezin dördüncü bölümünde GaToroid'in özellikleriyle beraber, FLUKA benzetim programı ve Flair arayüzü hakkında genel bilgi yer almaktadır. Tıp, kozmik ışınlar ve zırhlama gibi birçok kullanım alanına sahip FLUKA, radyasyonun madde içerisindeki etkileşim ve taşınımını simüle eder. Bu kısımda ayrıca GaToroid ile aynı ölçülere sahip bir kopyasının Flair programıyla tasarlanmasının ara aşamaları genel hatlarıyla verilmiştir. FLUKA programında kullanılan kartlar ve manyetik alan tanımlaması konusunda bilgi yine bu bölümde bulunmaktadır.

Tezin sonuçlar kısmında toroidal gentri için hesaplanan manyetik alanın proton demeti üzerine etkisi analiz edilmiştir. Farklı enerjilerindeki protonların *izomerkez* adı verilen tedavi noktasına odaklanabilmesi hızlandırıcıdan gelen proton demetlerinin GaToroid'e giriş açıları tespit edilmiştir. Son olarak da toroidal gentrinin performans değerlendirmesi doz dağılımı, lineer enerji transferi ve enerji depolanması gibi niceliklerin analiziyle yapılmıştır.

Son bölümde ise bu çalışmadan elde edilen ana bulgular sunulmuş, toroidal gentrinin klinik uygulamalarda kullanım potansiyeli tartışılmış ve gelecekte bu konuda yapılabilecek çalışmalar konusunda kısa bilgi verilmiştir.

1. RADIATION PHYSICS

1.1. Introduction

The term "radiation" encompasses a vast spectrum, including all forms of electromagnetic waves and the multitude of atomic and subatomic particles. The mechanisms governing these entities at the fundamental level are explored within the field of radiation physics. A core tenet of this field involves comprehending how matter interacts with radiation and the resultant effects.

Hadron therapy, which utilizes hadrons for cancer treatment, relies on crucial interactions between the hadrons and the irradiated tissue at therapeutic energies. These interactions can lead to the ionization or non-ionization of atoms and molecules within the medium.

Non-ionizing radiation is characterized by longer wavelengths ($\lambda \geq 10$ nm) within the electromagnetic spectrum. This category includes radio waves, microwaves, visible light, and ultraviolet light ($\lambda = 770$ nm to 10 nm).

In contrast, ionizing radiation occupies the higher-energy end of the spectrum. It comprises x-rays ($\lambda = 0.01$ to 10 nm) and gamma rays with shorter wavelengths. Additionally, it encompasses all atomic and subatomic particles such as electrons, positrons, protons, alpha particles, neutrons, heavy ions, and mesons.

This chapter focuses solely on ionizing radiation, which can be categorized into three main groups:

- Photons: Gamma rays (γ) and x-rays

- Charged particles: Electrons (e^-), positrons (e^+), protons (p), deuterons (d), alpha particles (α), and heavy ions ($A > 4$)

- Neutrons (n)

1.2. Photons

Photons, fundamental particles with no mass or charge, are a form of electromagnetic radiation traveling at the speed of light. Their energy and wavelength are related by a specific equation:

$$E = h\nu = h\frac{c}{\lambda} \tag{1.1}$$

where ν represents the photon's frequency and λ denotes its wavelength, h is Planck's constant and c is the speed of light.

Atoms can generate photons through various processes like excitation, ionization, or bremsstrahlung radiation. Traditionally, a distinction was made between x-rays (lower energy) and gamma rays (higher energy), but both are classified as photons in modern physics.

Photons interact with matter through various mechanisms, including photoelectric absorption, Compton scattering, and pair production.

1.2.1. Photoelectric absorption

The photoelectric effect describes the interaction between a photon and a bound atomic electron. This interaction causes the photon to be absorbed, leading to the ejection of an atomic electron, which becomes a free electron known as a photoelectron (Figure.1.1). The kinetic energy of a photoelectron equals:

$$E_{e^-} = E_\gamma - E_b \tag{1.2}$$

where E_γ energy of incident photon and E_b is binding energy of electron.
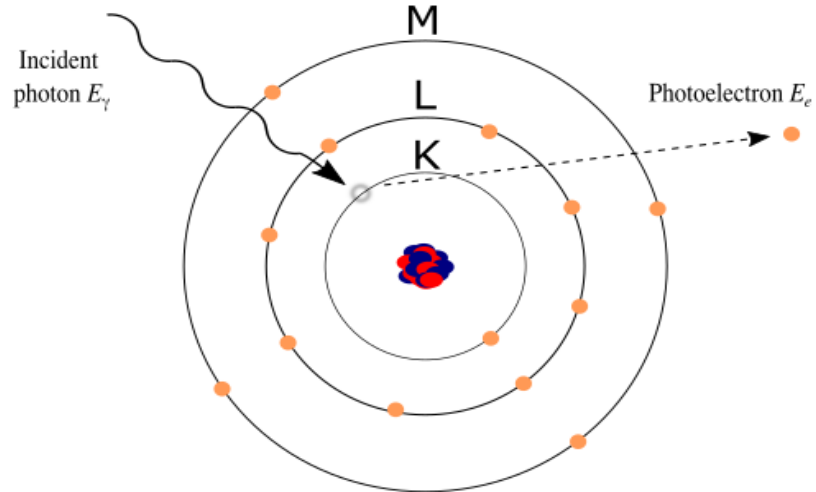
Figure 1.1. Photoelectric effect: Interaction of a Photon with a Bound Electron.

The probability of photoelectric absorption is quantified by the photoelectric coefficient, also known as the photoelectric cross-section, τ [1]. This coefficient is represented by the following equation:

$$\tau[m^{-1}] \propto \frac{Z^n}{E_\gamma^{3.5}} \tag{1.3}$$

where Z is atomic number of the target material, and n is a constant with value of 3-5 depending on the photon energy E_γ.

Equation 1.3 highlights the dependence of the photoelectric effect on both the atomic number (Z) and the photon energy (E_γ). The photoelectric process has a strong dependence on the atomic number, with materials possessing higher Z values exhibiting a greater probability of photoelectric absorption. Additionally, the proportionality to Z^n indicates that the photoelectric effect is dominant at lower photon energies ($E_\gamma < 0.25$ MeV). This is because lower-energy photons are more readily absorbed by the tightly bound electrons of high-Z materials, leading to their complete ejection from the atom.

1.2.2. Compton scattering: photon-electron collision

Compton scattering describes the interaction between a photon and a relatively free electron (see Figure 1.2). Electrons are typically bound, if their binding energy is on the order of eV, they are considered free. During Compton scattering, the incident

photon with energy E_γ in order keV collides with the electron, transferring some of its energy to the electron and deflecting the photon at an angle θ.

The energy (E'_γ) of the scattered photon after the collision can be calculated using the Compton scattering formula:

$$E'_\gamma = \frac{E_\gamma}{1 + \frac{E_\gamma}{mc^2}(1 - \cos\theta)} \tag{1.4}$$

where E_γ represents the initial energy of the incident photon, mc^2 ($\sim$ 0.511 MeV) signifies the rest of mass energy of the electron, and θ denotes the scattering angle.

The conclusion of equation 1.4 is that the minimum energy of the scattered photon is always nonzero. This implies that the electron cannot absorb all the energy from the incident photon in a Compton scattering event. The transferred energy is deposited within the material over a distance corresponding to the electron's range, while the scattered photon may potentially escape the medium.

The probability of Compton scattering occurring is quantified by the Compton cross-section (σ) [2]:

$$\sigma[m^{-1}] = NZf(E_\gamma) \tag{1.5}$$

Here, N is the atom density of the target material, and f is a function of E_γ. Through simplifications, this equation can be approximated as:
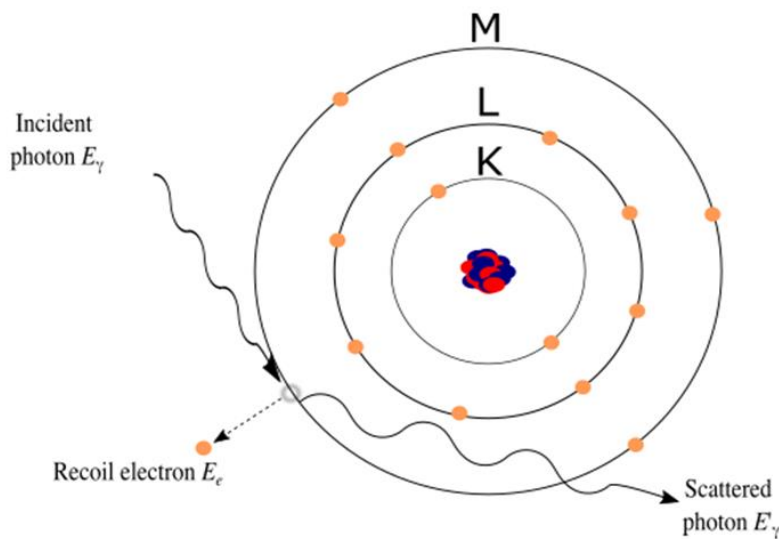
Figure 1.2. Compton scattering: Interaction between a photon and a free electron.

$$\sigma[m^{-1}] \sim \rho \left(\frac{N_A}{A}\right) \frac{A}{2} f(E_\gamma) \sim \rho \frac{N_A}{2} f(E_\gamma) \qquad (1.6)$$

According to equation 1.6, the probability of Compton scattering is relatively independent of the target material's atomic number.

1.2.3. Pair production: photon-nucleus interaction

Pair production involves a high-energy photon interacting with a nucleus, leading to the disappearance of the photon and the creation of an electron-positron pair. The rest mass of electron or positron equal to 0.511 MeV. Due to the energy required to create these particles, there exists a minimum energy threshold for the incident photon. This minimum energy, as dictated by the principle of mass-energy equivalence ($E = mc^2$), is 1.022 MeV. Photons with energies lower than this threshold cannot undergo pair production. (see Figure 1.3).
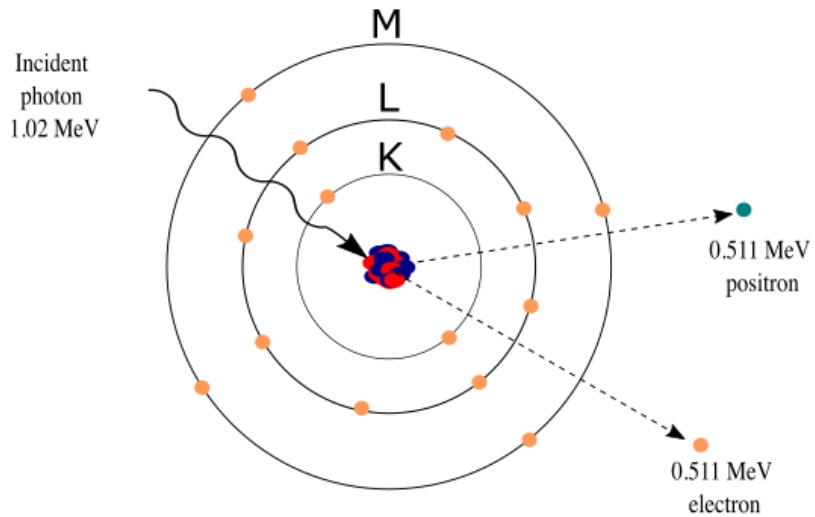
Figure 1.3. Pair production: Photon-nucleus interaction and minimum energy threshold for electron-positron creation.

The probability of pair production, quantified by the pair production coefficient or cross section, is a complex function of both the incident photon energy ($E\gamma$) and the atomic number (Z) of the target material [2]:

$$\kappa[m^{-1}] = NZ^2 f(E_\gamma, Z) \qquad (1.7)$$

5

where $f(E\gamma, Z)$ is a function that exhibits a slight dependence on Z and an increasing trend with increasing $E\gamma$.

1.2.4. Total photon attenuation coefficient

The total probability of a photon interacting with matter along a unit path length is quantified by the total linear attenuation coefficient, denoted by the symbol μ. This coefficient represents the sum of all possible interaction mechanisms a photon can undergo within a material, including photoelectric absorption, Compton scattering, and pair production (as discussed previously). Mathematically, μ is expressed as the sum of individual probabilities for each interaction type.

$$\mu[m^{-1}] = \tau + \sigma + \kappa \tag{1.8}$$

where τ signifies the photoelectric absorption coefficient, σ represents the Compton scattering coefficient, and κ denotes the pair production coefficient. Physically, μ is the probability of interaction per unit distance.

The mass attenuation coefficient (μ_m), provides a material-independent measure of the interaction probability between photons and matter. It is obtained by normalizing the linear attenuation coefficient with the material's density (ρ):

$$\mu_m[\text{m}^2/\text{kg}] = \frac{\mu}{\rho} \tag{1.9}$$

The mass attenuation coefficient is an important parameter for evaluating the suitability of a material for photon shielding applications [1]. Materials with lower μ_m values are more likely to allow photons to pass through with minimal interaction, making them less effective for shielding purposes.
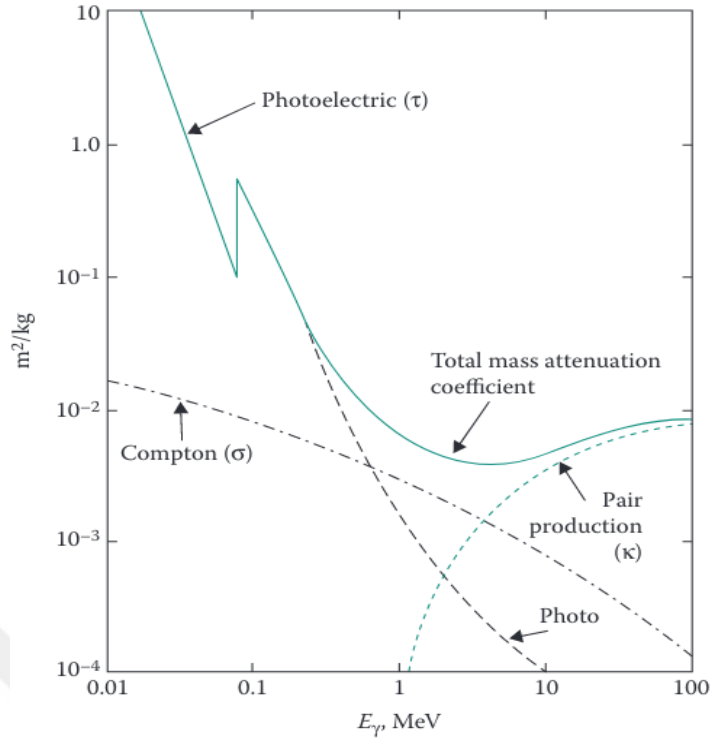
Figure 1.4. Mass attenuation coefficient: Photon interaction probability in lead (Pb)[2].

When a collimated beam of mono-energetic photons (all having the same energy) with initial intensity I_0 strikes a material with thickness x, the number of photons (I) exiting the material without interacting can be described by the following equation:

$$I = I_0 e^{-\mu x} \tag{1.10}$$

where μ is the total linear attenuation coefficient. The term $e^{-\mu x}$ in equation 1.10 signifies the probability of a photon traversing a material of thickness x without undergoing any interaction. This probability can be expressed as:

$$T = \frac{I}{I_0} = e^{-\mu x} \tag{1.11}$$

Another useful quantity is the mean free path (λ) that represents the average distance a photon travels within the material before experiencing its first interaction. It can be calculated using the following relationship:

$$\lambda[m] = \frac{\int_0^\infty x e^{-\mu x} dx}{\int_0^\infty e^{-\mu x} dx} = \frac{1}{\mu} \tag{1.12}$$

7

The mean free path is inversely proportional to the total linear attenuation coefficient (μ). It quantifies the average distance a particle travels within the material before undergoing a significant interaction event. This distance signifies the range over which the particle's behavior can be predicted statistically using a non-interacting model.

1.3. Charged Particles

In contrast to γ-rays, which deposit their energy through a limited number of interactions with matter, charged particles experience continuous energy loss via numerous interactions throughout their trajectory. These interactions, dominated by Coulomb forces, eventually bring the charged particle to a complete stop within a limited distance known as its range.

1.3.1. Coulomb interactions with electrons and nuclei

As charged particles traverse a material, they interact with the constituent atoms. These interactions primarily occur with either the atomic electrons or the nucleus. While simplified analysis suggests a higher probability of collisions with electrons due to their abundance than nuclei, both interactions play a role. The charged particle's presence exerts a Coulomb force on the atomic electrons. This force can transfer energy from the moving particle to a bound electron, leading to ionization or excitation (Figure 1.5).
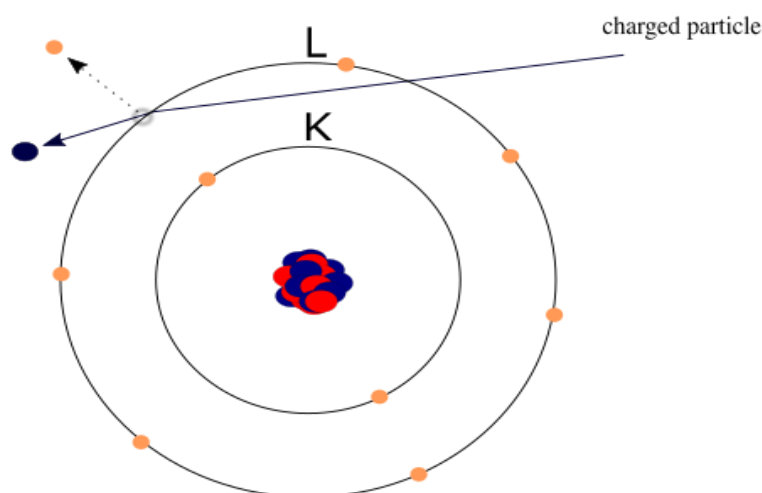
Figure 1.5. Coulomb interaction between the charged particle and atomic electron leads to ionization.

- **Ionization:**

  The electron gains sufficient energy to overcome its binding energy and escape the atom, becoming a free electron with kinetic energy. These freed electrons, often called delta rays (δ-rays), can ionize other atoms through subsequent interactions.

- **Excitation:**

  The electron absorbs energy but remains bound to the atom, transitioning to a higher energy orbital. The excited atom then releases this excess energy as a characteristic x-ray when the electron returns to a lower energy state (Figure 1.6).

Interactions resulting in ionization or excitation are classified as inelastic collisions.
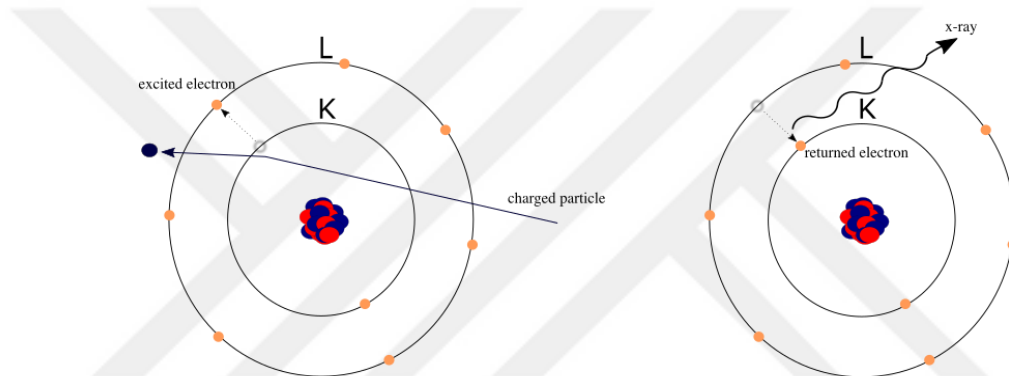
Figure 1.6. Atomic excitation (left) and subsequent x-ray emission (right).

Additionally, charged particles moving through matter may experience elastic collisions with nuclei or atomic electrons, where energy is conserved for kinetic energy and linear momentum. However, these elastic collisions are not significant for the energy loss of charged particles.

1.3.2. Bremsstrahlung: Radiation due to charged particle acceleration

Bremsstrahlung, derived from the German meaning "braking radiation," refers to the electromagnetic radiation emitted when a free-charged particle accelerates or decelerates, leading to a radiative energy loss, as shown in Figure 1.7.

Unlike monoenergetic radiation, bremsstrahlung photons emit a continuous spectrum of energies ranging from zero up to a maximum equivalent to the kinetic energy of the moving charged particle, which can either be reabsorbed within or escape from the material.
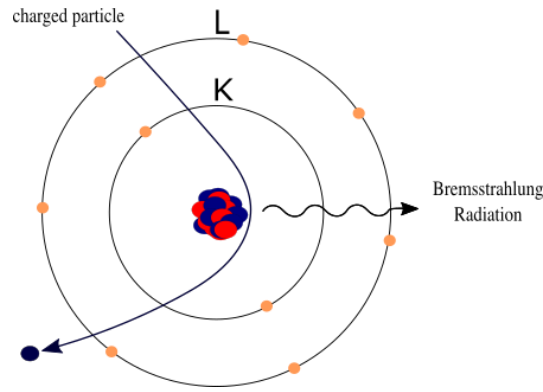
Figure 1.7. Illustration of Bremsstrahlung radiation.

Consider a charged particle with charge *ze,* and mass *M* moving within a material with atomic number *Z*. The Coulomb force between the particle and a nucleus of the material is $F \sim zeZe/r^2$, where *r* represents the distance between the charges. The resultant acceleration of the charged particle is $a = F/M \sim zZe^2/M$. Indeed, an accelerating charge radiates energy in proportion to the square of its acceleration. Consequently, the intensity of the emitted bremsstrahlung radiation *I* is:

$$I \propto a^2 \sim \left(\frac{zZe^2}{M}\right)^2 \sim \frac{z^2 Z^2}{M^2} \tag{1.13}$$

Among particles traversing the same medium, the lighter particle emits significantly more bremsstrahlung than the heavier particle, assuming other factors remain constant. Also, more bremsstrahlung is emitted when a particle travels through a medium with a higher atomic number, *Z*, than one with a lower atomic number.

For charged particles with energies considered here, the kinetic energy lost as bremsstrahlung is primarily significant for electrons. However, it becomes particularly relevant for electrons in high-*Z* materials such as lead ($Z = 82$).

1.3.3. Nuclear interaction

Charged particles interact with atomic nuclei through various mechanisms. This section will focus on two main categories of these interactions:

1.3.3.1. Elastic scattering

The incident particle collides with the nucleus in elastic scattering and deflects from its original trajectory (Figure 1.8). This process resembles a billiard ball collision, where the total momentum of the system is conserved. However, unlike billiard balls,

the much heavier nucleus typically retains its original kinetic energy, while the incident particle may experience a slight change in its energy due to the difference in masses.
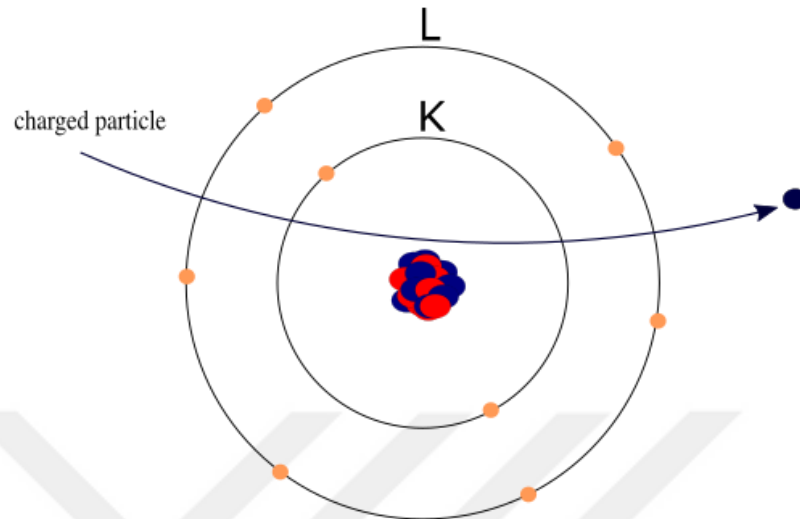
Figure 1.8. Elastic scattering of a charged particle by the nucleus.

1.3.3.2. Inelastic scattering

Inelastic scattering occurs when the incident particle transfers a portion of its kinetic energy to the target nucleus. This energy transfer can excite the nucleus to a higher energy state or even induce nuclear reactions. These reactions result in the emission of secondary particles, such as protons, neutrons, or other nuclear fragments (see Figure 1.9).
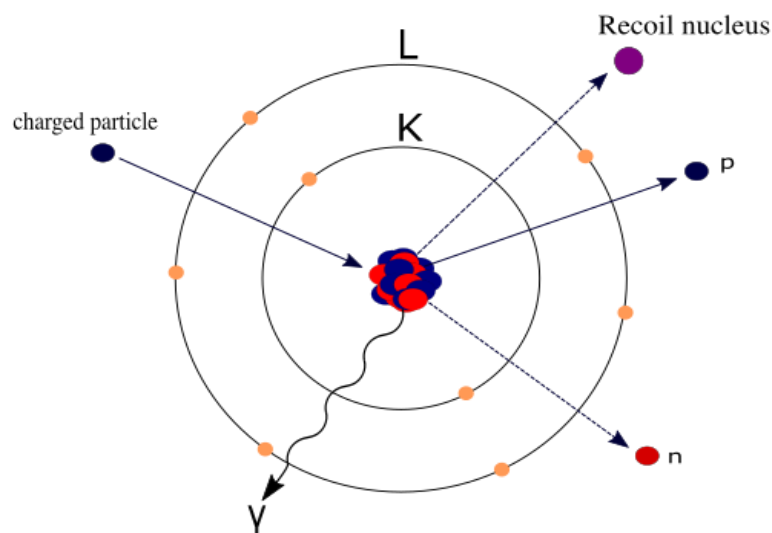
Figure 1.9. Inelastic scattering of charged particle by nucleus with secondary particle emission.

1.3.4. Cherenkov radiation

Cherenkov radiation was discovered by Pavel Cherenkov in 1934, is a fascinating phenomenon that occurs when a charged particle, such as an electron or a proton, travels through a medium at a speed exceeding the speed of light in that medium. This situation might seem impossible, but it's important to remember that light speed can be slower in certain materials compared to a vacuum.

As the charged particle traverses the medium, it disrupts the surrounding electric field, momentarily polarizing the atoms or molecules in its path. This rapid polarization creates a localized electromagnetic disturbance. When the disturbance propagates, it emits light as a cone-shaped wavefront centered around the particle's trajectory. The emitted photons have a characteristic bluish hue and travel at the speed of light within the medium. The intensity and emission angle of the Cherenkov radiation depends on several factors:

- **Particle Velocity:** Higher particle velocities relative to the light speed in the medium lead to a stronger and more narrowly focused cone of emitted radiation.
- **Medium Refractive Index:** Materials with a higher refractive index result in a narrower emission cone angle. Water (used in nuclear reactors) and certain plastics are commonly used media for Cherenkov radiation detection.
- **Particle Path Length:** The total distance the particle travels within the medium influences the overall intensity of the emitted radiation.

Despite being a minor contributor to a charged particle's energy loss, Cherenkov radiation offers valuable applications across scientific disciplines. In particle physics experiments, Cherenkov detectors identify and measure the velocities of high-energy particles produced in accelerators. Medical imaging techniques like Positron Emission Tomography (PET) scans leverage Cherenkov radiation emitted by positrons to create detailed maps of metabolic activity within the body. Furthermore, high-energy astrophysics utilizes Cherenkov telescopes to detect the faint Cherenkov radiation produced by cosmic ray particles interacting with Earth's atmosphere, aiding our understanding of high-energy phenomena in the cosmos.

1.4. Neutron

Neutrons are uncharged subatomic particles with a mass very similar to that of positively charged protons. This lack of electrical charge prevents neutrons from directly ionizing atoms and molecules within tissue. However, their role in radiation therapy (RT) is significant due to their ability to interact with atomic nuclei.

When neutrons collide with atomic nuclei, particularly those of hydrogen (abundant in human tissue), they transfer a portion of their kinetic energy. This energy transfer can cause the struck nucleus to recoil, creating a secondary form of ionization within the surrounding biological material. Additionally, neutron interactions can lead to the emission of various subatomic particles, recoil nuclei, and photons. These secondary particles deposit their energy in diverse ways, ultimately resulting in various biological effects within irradiated tissues.

In the field of RT, neutrons are categorized based on their inherent energy levels. Slow neutrons, also known as thermal neutrons, exhibit energies of approximately 0.025 eV. Conversely, fast neutrons have significantly higher energy levels, typically within the keV and MeV range [3]. This distinction in energy spectrum demonstrably influences the efficacy of treatment and the spectrum of biological effects observed.

Neutron therapy, a modality for cancer treatment, utilizes neutrons as its therapeutic agent. Two primary forms exist fast: neutron therapy (FNT) and boron neutron capture therapy (BNCT). FNT leverages fast neutrons to directly inflict damage upon cancer cells. In contrast, BNCT relies on the selective uptake of boron atoms by cancer cells. Subsequently, these boron-laden cells are bombarded with thermal neutrons (Figure 1.10), inducing the boron to release energy and thereby eradicate the cancer cells [4]. Both FNT and BNCT have been under development since the 1930s.
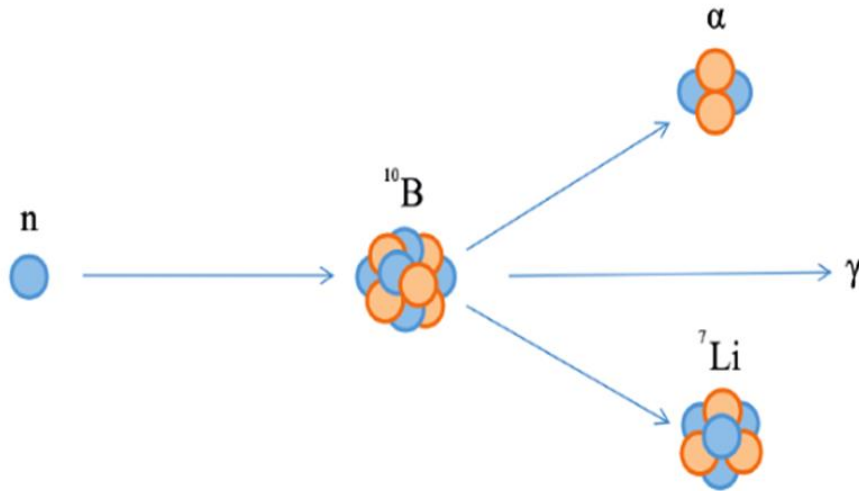
Figure 1.10. Energy release in ^{10}B: ^{10}B(n, γ)^{7}Li reaction depicted.

1.5. Stopping Power

A charged particle moving through a material simultaneously exerts Coulomb forces on many atoms. Every atom has many electrons with different ionization and excitation potentials. As a result of this, the moving charged particle interacts with a tremendous number of electrons—millions. Each interaction has its own probability of occurrence and a certain energy loss. It is impossible to calculate the energy loss by studying individual collisions. Instead, an average energy loss is calculated per unit distance traveled. The average energy loss per unit distance traveled by the particle or a stopping power (S) is:

$$S = -\frac{1}{\rho}\frac{dE}{dx}(\text{MeVcm}^2/\text{g})\tag{1.14}$$

where ρ is the density of the material, and dE/dx is stopping power, the minus sign makes S positive. The stopping power calculation is given by Bethe–Bloch equations [2], [4]:

1. for p, d, t, α

$$S = 0.307z^2\frac{Z}{A\beta^2}\left[ln\left(\frac{2m_ec^2\beta^2}{I(1-\beta^2)}\right) - \beta^2 - \frac{\delta}{2} - \frac{U}{2}\right]\tag{1.15}$$

2. for electrons

$$S = 0.307z^2 \frac{Z}{A\beta^2} \left\{ ln \left(\frac{\beta\gamma\sqrt{\gamma-1}}{I} m_e c^2 \right) \right.$$
$$\left. + \frac{1}{2\gamma^2} \left[\frac{(\gamma-1)^2}{8} + 1 - (\gamma^2 + 2\gamma - 1) \ln 2 \right] - \frac{\delta}{2} - \frac{U}{2} \right\}$$

(1.16)

3. for positrons

$$S = 0.307z^2 \frac{Z}{A\beta^2} \left\{ ln \left(\frac{\beta\gamma\sqrt{\gamma-1}}{I} m_e c^2 \right) \right.$$
$$\left. + \frac{\beta^2}{24} \left[23 + \frac{14}{\gamma+1} + \frac{10}{(\gamma+1)^2} + \frac{4}{(\gamma+1)^3} \right] + \frac{\ln 2}{2} - \frac{\delta}{2} - \frac{U}{2} \right\}$$

(1.17)

$m_e c^2$: rest mass energy of the electron = 0.511 MeV

$$\gamma = 1 + \frac{T}{Mc^2} = \frac{1}{\sqrt{1-\beta^2}}$$

where T is kinetic energy, and M is the rest mass of the particle.

$\beta = v/c$, c : speed of light in vacuum = 2.997930×10^8 m/s $\approx 3 \times 10^8$ m/s

Z and A : atomic number and atomic mass of the material

z : charge of the incident particle ($z = 1$ for $e-$, $e+$, p, d; $z = 2$ for α)

I : mean ionization or excitation potential of the material

δ : density effect correction

U : shell effect correction

1.6. Range

The total distance a charged particle travels within a material before coming to a complete stop is referred to as its range. This stopping distance is influenced by various factors, as described by equations 1.15 to 1.17. These factors include:

- **Particle Properties:** The mass, velocity, and initial kinetic energy of the incident charged particle.
- **Material Properties:** The density and atomic number (Z) of the material the particle traverses.

The unit of the range is meter; The dependency of material state can be eliminated by changing the unit to kg/m^2 or g/cm^2 with:

$$R[\text{kg/m}^2] = R[\text{m}]\rho[\text{kg/m}^3] \tag{1.18}$$

where R denotes the range and ρ represents the density of the material. Thus, a particle will have the same range in kg/m^2 whether it travels through ice, water, or steam. However, the range measured in meters will be diffrent.

It's important to note that the range is an average value. Particles of the same type and initial kinetic energy traversing the same material may not all stop at precisely the same depth. Their actual path lengths (pathlengths) can exhibit some variation. The range is given by

$$\bar{R} = \int_{E_0}^{0} -\frac{dx}{dE}\, dE = \int_{0}^{E_0} \frac{dE}{-dE/dx} = \int_{0}^{E_0} \frac{dE}{S} \tag{1.19}$$

where $\bar{R}$ is the average range and E_0 is the initial energy of the particle.

1.7. Dose

In particle therapy (PT), dose calculation is conducted to determine the dose distribution within a patient's body.

1.7.1. Absorbed dose

The absorbed dose typically refers to the amount of energy absorbed per unit mass by a material or a biological tissue. This can accure during exposure to ionaizing radiation. The SI dose unit is gray (Gy), and 1Gy = 1 J/kg. The absorbed dose can be estimated by [5]:

$$D(E, z) = \frac{S_{el}(E)\Phi(E, z)}{\rho(z)} \tag{1.20}$$

Here, $\rho(z)$ represents the mass density of the current medium in which energy is deposited. This calculation involves the utilization of two essential factors: electronic stopping power ($S_{el}(E)$) and fluence ($\Phi(E, z)$).

1. **Electronic Stopping Power:** This refers to the rate at which charged particles lose kinetic energy as they traverse through a material due to interactions with

the electrons of the medium. By quantifying this stopping power, one can determine how much energy the particles deposit as they penetrate a substance.

2. **Fluence:** Fluence describes the number of particles passing through a unit area per unit time. It provides information about the density of particles present in a given region.

1.7.2. Equivalent dose

The different types of radiation caused different biological effectiveness on the body, called as equivalent dose. This equivalent dose to a tissue T, exposed to different radiation types R, is defined as:

$$H_T = \sum W_R D_{T,R} \qquad (1.21)$$

where W_R is the radiation weighting factor and $D_{T,R}$ is the absorbed dose in tissue T from radiation R. The unit of H is Sievert (Sv) in the International System of Units.

1.7.3. Effective dose

Besides the variances in biological responses to radiation exposure, it is essential to consider the distinct reactions of various tissues and organs to different types of radiation. The effective dose is defined as:

$$H_E = \sum W_R H_T \qquad (1.22)$$

where W_R is the radiation weighting factor, H_T is the equivalent dose.

1.8. Bragg Peak

When charged particles, such as protons, are directed into tissue, they lose energy as they interact with atoms along their path. This energy loss increases as the particles slow down. However, just before they come to a complete stop, they release a significant portion of their remaining energy in a narrow region known as the Bragg Peak (Figure 1.11 [6]). Bragg Peak represents the maximum energy deposition of the charged particles within the tissue [7].

For protons and heavy ions, such as carbon, the radiation dose increases as they traverse through tissue, steadily releasing energy (i.e., the dose escalates with greater

tissue depth until reaching the Bragg Peak), typically occurring near the particle's maximum penetration depth. Beyond the Bragg peak, at the end of the irradiation, the dose for protons drops to zero, and for heavy ions, it becomes nearly zero. This leads to the absence of an exit dose compared to photon irradiation. Additionally, fewer healthy tissues are exposed to radiation at the beginning of the path, as shown in Figure 1.11. Overall, charged particles significantly reduce radiation dose compared to photons, making them preferable for cancer treatment. Positioning tumors at the Bragg peak location makes it possible to effectively destroy them while preserving healthy tissues.
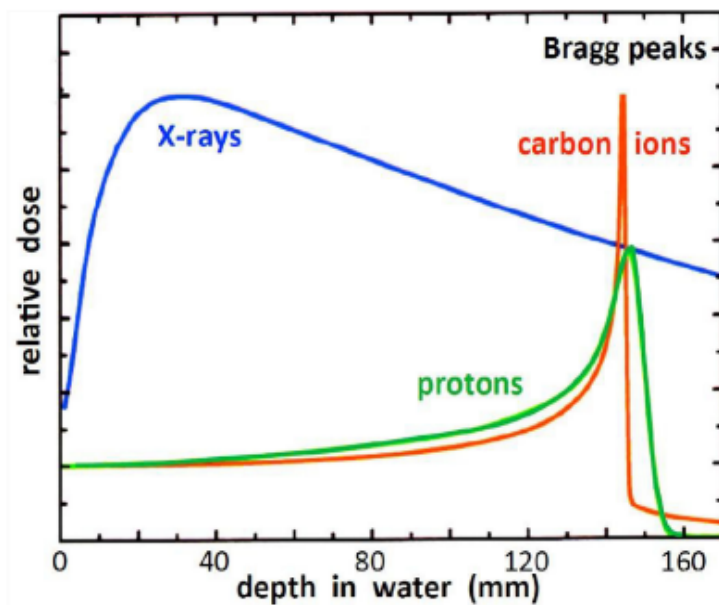
Figure 1.11. Bragg peaks for protons and carbon ions.

1.9. Linear Energy Transfer

Particle beams exhibit greater biological effectiveness than photon beams, even when administered at equivalent physical doses, owing to their energy transfer mechanism. This transfer of energy in particle beams is quantified as linear energy transfer (LET). LET represents the average energy transfer per unit length (unit: keV/µm), traveled by charged particles through electronic interactions such as ionization or excitation. Its measurement is determined using the Bethe equation.

Two practical concepts, LET_t and LET_d, have been developed based on the original definition of LET.

1.9.1. Track-averaged LET

LET$_t$, or Track-Averaged Linear Energy Transfer, is determined by averaging the energy dissipated by charged particles throughout their trajectory. This calculation offers an understanding of the density of ionization occurring along the particle's path. It represents the mean value derived from the fluence spectrum of LET [8].

$$LET_t(z) = \frac{\int_0^\infty S_{el}(E)\Phi(E,z)dE}{\int_0^\infty \Phi(E,z)dE} \quad (1.23)$$

where $S_{el}(E)$ represents the electronic stopping power of primary charged particles with kinetic energy E, and $\Phi(E,z)$ denotes the fluence of primary charged particles with kinetic energy E at position z.

High LET$_t$ values indicate that the radiation deposits a significant amount of energy over a short distance, which is typical for heavy charged particles like carbon ions [9]. These high LET radiations are more effective at causing dense ionization clusters along their tracks, leading to more significant biological damage. In contrast, low LET$_t$ values are characteristic of lighter particles such as electrons, positrons or photons, which tend to deposit energy more sparsely along their path.

Understanding LET$_t$ is crucial for predicting the relative biological effectiveness (RBE) of different types of radiation, as high LET radiation generally has a higher RBE due to its dense ionization. RBE of protons is typically assumed to be 1.1, but it is, in fact, variable and influenced by factors such as proton energy, dose per fraction, tissue and cell type, and end point [10].

1.9.2. Dose-averaged LET

Substituting dose for particle flux in equation 1.23 yields the dose-averaged LET (LET$_d$) [8]:

$$LET_d(z) = \frac{\int_0^\infty S_{el}(E)D(E,z)dE}{\int_0^\infty D(E,z)dE} = \frac{\int_0^\infty S_{el}^2(E)\Phi(E,z)dE}{\int_0^\infty S_{el}(E)\Phi(E,z)dE} \quad (1.24)$$

where $S_{el}(E)$ is the electronic stopping power of primary charged particles with kinetic energy E, and $D(E,z)$ denotes the absorbed dose contributed by primary charged particles with kinetic energy E at position z. The concluding segment of this equation

is derived by substituting the absorbed dose from equation 1.20, a step facilitating Monte Carlo calculations.

Since relative dose is the weighting factor in computing this averaged LET, it is termed dose-averaged LET. Essentially, when particles travel similar lengths, a track with a high LET can impart a greater dose than one with a low LET. Consequently, it's reasonable to infer that a high-LET track may exert a more pronounced effect on cell destruction, implying a greater biological effect.

2. HADRON THERAPY

2.1. Introduction

The fight against cancer is a continuous struggle, and while existing therapies like surgery, chemotherapy, and immunotherapy have proven to be effective, they are not without limitations. Hadron therapy emerges as a promising new frontier in cancer treatment. Its development is deeply intertwined with advancements in medical physics, building upon groundbreaking discoveries that have revolutionized our understanding of radiation therapy.

Following Wilhelm Röntgen's discovery of x-rays in 1901, Marie Curie's pioneering work on radioactivity laid the foundation for understanding subatomic particles like protons, crucial for hadron therapy. Further advancements, including the invention of the cyclotron by Ernest Lawrence, paved the way for the development of particle accelerators used in hadron therapy. These discoveries culminated in proton therapy, offering a more targeted approach than conventional methods.

The unique advantage of proton therapy is its characteristic depth-dose distribution, called the Bragg peak (Section 1.8). This phenomenon refers to the point within the tissue where protons lose their maximum energy [7]. This precise energy deposition allows for highly targeted treatment of tumors, minimizing damage to surrounding healthy tissues. However, the widespread adoption of proton therapy faces challenges due to current infrastructure limitations. Treatment facilities require large, specialized equipment, leading to significant size and cost barriers.

In hadron therapy, the particle beams undergo a complex process, from the source of charged particles to their interaction within the patient's body, targeting and destroying cancerous tumors. The accuracy and speed at each stage are crucial for optimizing treatment and maintaining medical devices. Notably, this operation involves various sensitive and intricate devices. Enhancing each step ensures effective treatment and significantly reduces treatment costs. Consequently, advancements in hadron therapy

hold the potential to benefit a wider range of patients from this treatment method. The following sections will summarize each of the aforementioned steps.

2.2. Treatment Process

2.2.1. Ion source

An ion source is designed to create and extract charged particles (ions) from a gas. These ions can be either positively or negatively charged. Charged particles, like protons, helium, and carbon, exhibit a high rate of energy loss along their track, resulting in high biological effectiveness and making particle therapy particularly attractive for cancer treatment [11]. Beyond traditional applications in cancer treatment, new ion species like helium, lithium, boron, oxygen, neon, argon, and iron hold promise for bio-spatial research [12].

2.2.1.1. Ion source selection

The selection of an ion source for hadron therapy applications is a multi-faceted decision influenced by several key parameters. These parameters include:

- **Acceleration Efficiency:** The source's ability to generate ions suitable for efficient acceleration within the specific therapeutic energy range (typically 70-250 MeV for protons).
- **Treatment Efficiency:** The source's contribution to the overall treatment process impacts beam current and stability, influencing treatment delivery times and effectiveness.
- **Cost-Effectiveness:** The source's acquisition and operational costs include maintenance requirements and resource consumption.
- **Ease of Preparation and Availability:** The practicality of preparing and maintaining the ion source within a clinical setting, its commercial availability, and its potential for reliable operation.

2.2.1.2. Proton and carbon ion sources

A strong electrical discharge rips apart hydrogen gas (H_2) molecules in an ion source. This tears away electrons, leaving behind the positively charged protons that are the

building blocks for proton therapy. These protons are desirable because hydrogen is abundant and the ionization process is relatively simple [13].

Conversely, carbon ions, another prevalent choice due to their advantageous biological properties, are typically derived from carbon dioxide (CO_2). Notably, carbon ions exhibit a desirable coincidence between the Bragg peak (maximum energy deposition) and their relative biological effectiveness (increased cell-killing efficiency). Additionally, they boast low oxygen enhancement ratios, meaning their effectiveness is less affected by the presence or absence of oxygen in the tumor microenvironment [14]. This combination of characteristics makes carbon ions particularly attractive for specific cancer treatment applications.

Hadron beam therapy is revolutionizing with exploring laser plasma as a next-generation ion source. This innovative approach offers several exciting advantages over conventional accelerators. Laser-plasma sources are significantly more compact, making them easier to integrate into treatment facilities. Additionally, this technology simplifies the process of delivering ions to the treatment room. Finally, by designing specialized targets, researchers can tailor the ion beam to meet the precise dosimetric requirements critical for safe and effective radiation therapy [15].

2.2.2. Accelerators

While particle accelerators play a pivotal role in various subatomic physics disciplines, particularly high-energy particle physics research conducted at facilities like CERN, their application in hadron therapy necessitates a different approach [16]. Therapeutic applications require accelerators that produce particle beams within a specific energy range. These accelerators are considerably less complex than their high-energy counterparts used in fundamental research [17], [18]. Despite these differences, significant advancements have been made in harnessing the therapeutic potential of charged particles like protons.

Currently, hadron therapy facilities rely on circular accelerators like cyclotrons and synchrotrons. While both can accelerate protons, only synchrotrons have the capability for heavier ions like carbon due to their higher energy requirements [19].

2.2.2.1. Cyclotrons

Accelerators operate by exerting the Lorentz force on charged particles. Utilizing this principle, Ernest O. Lawrence and M. Stanley Livingston developed the cyclotron, the first charged particle accelerator, in the early 1930s.

Cyclotrons offer advantages such as compactness and higher beam intensity due to their continuous proton stream. An example of a cyclotron, the PSI 590-MeV ring cyclotron in Switzerland, is given in Figure 2.1. To achieve lower energy levels, protons accelerated to the cyclotron's maximum energy undergo degradation through energy degraders.
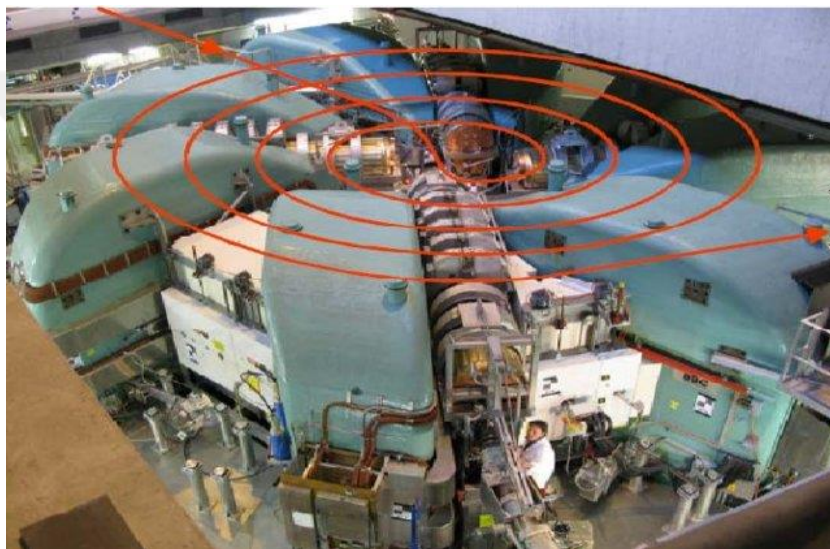
Figure 2.1. The PSI 590-MeV ring cyclotron: The schematic illustrates the beam path from the 72-MeV Injector.

2.2.2.2. Synchrotrons

A new concept in circular accelerators involves dynamically varying the magnetic field of the bending magnets. The magnetic field is proportionally increased as particles accelerate to match their energy. Therapy synchrotrons produce beams with relatively low intensity and adjustable energy. Protons ($\sim 10^{11}$ primary protons) or carbon ions ($\sim 10^9$ primary carbons) are injected into a ring of dipole magnets at 2-7 MeV/u and then accelerated to the desired energy in 1 second [20]. The injection begins with an ion source, progresses through a linear accelerator, and then moves to a synchrotron with diameters of up to 20 meters. By accelerating batches of protons to the desired energies, synchrotrons achieve a smaller energy spread and lower power consumption. A prominent example of a synchrotron used for particle therapy is the

MedAustron facility located in Austria (Figure 2.2 [21]). This facility utilizes a synchrotron to deliver proton and carbon ion therapy for cancer treatment.

Synchrotrons provide adjustable energy but suffer from a dead time between cycles, hindering their use in treating organs with movement, such as the lungs during respiration or the heart throughout the cardiac cycle.

Figure 2.2. The MedAustron particle therapy accelerator facility.

2.2.2.3. Synchrocyclotron

Synchrocyclotrons are particle accelerators that stand out for their efficiency and size. They use strong magnetic fields to accelerate charged particles, making them well-suited for modern medical applications like proton therapy. IBA's S2C2, a cutting-edge superconducting synchrocyclotron, exemplifies this technology in their ProteusOne® system [22]. A schematic view of that system is given in Figure 2.3.

One drawback of synchrocyclotrons is their non-isochronous operation. This means that particles with different energies travel at slightly different speeds within the machine. To overcome this challenge and ensure all particles reach their target energy simultaneously, IBA developed sophisticated computational tools for the S2C2. These tools manage parameters like the movement of particles along the path (longitudinal beam physics), the varying radio frequency that propels them, and any unexpected effects (non-linearities) that might occur during operation.

Synchrocyclotrons offer a winning combination of efficiency, compactness, and control. IBA's S2C2 serves as a prime example, demonstrating how this technology, with its innovative design and advanced control systems, can pave the way for a more accessible and cost-effective future for proton therapy.
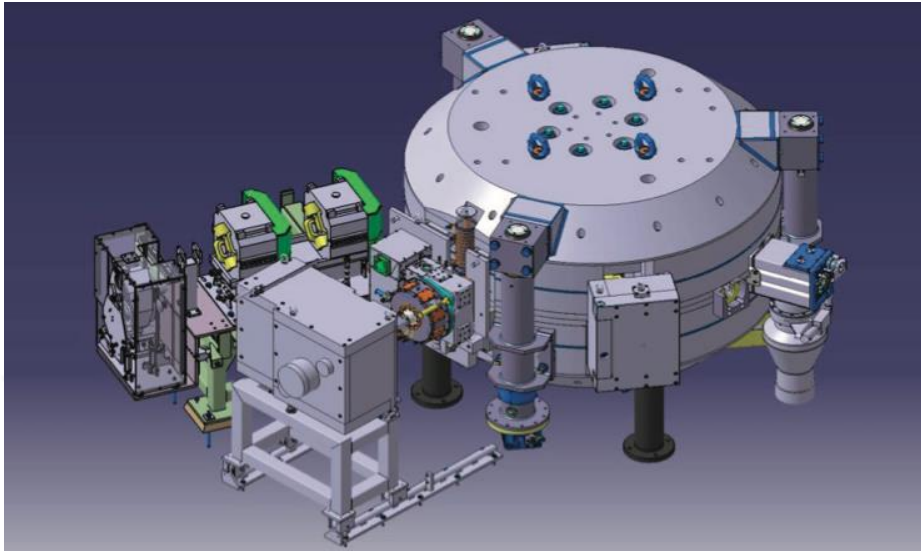
Figure 2.3. Schematic of the IBA S2C2 synchrocyclotron.

2.2.2.4. LINAC

Linear accelerators, or LINACs, are a long-established technology (invented in 1924) for accelerating particles in a straight line using an alternating electric field. Recently, a novel commercial system called LIGHT, under collaboration with CERN, has been introduced for the field of proton therapy. LIGHT utilizes a LINAC design, combining three sections into a single 25-meter accelerator. This system offers unique advantages compared to traditional methods. LIGHT's ability to rapidly switch the energy of its proton beam on a pulse-by-pulse basis makes it ideal for a precise targeting technique called "pencil beam scanning" in proton therapy. Furthermore, LIGHT minimizes beam loss and simplifies facility construction by eliminating the need for a beam degrader through fast energy switching, LIGHT minimizes beam loss and simplifies facility construction. These features make LIGHT a promising new technology for the future of spot-scanning proton therapy.
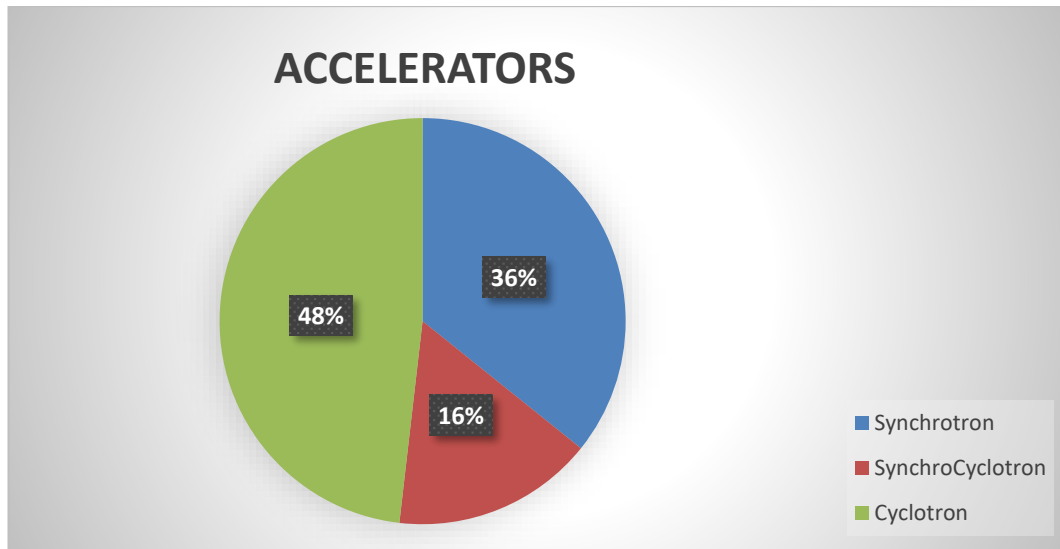
Figure 2.4. Distribution of accelerator technologies in global particle therapy facilities. Data source [PTCOG], (last update: May 2024).

Figure 2.4 illustrates the global distribution of three accelerator types employed within particle therapy facilities. These facilities provide treatment using beams of charged particles, primarily protons and heavier ions like carbon ions, for cancer therapy. As can be seen from the data, cyclotrons hold the dominant position, representing approximately 48% of all installations. Synchrotrons follow closely behind at 36%, while synchrocyclotrons constitute the remaining 16%.

Modern hadron therapy demands advancements in accelerator technology to achieve compactness and cost-effectiveness. This objective necessitates exploring alternative solutions beyond conventional cyclotrons and synchrotrons.

Two such promising avenues lie in Laser-Driven Plasma Wakefield Acceleration (LWFA) and Particle Beam-Driven Plasma Wakefield Acceleration (PWFA) [23]. LWFA utilizes intense laser pulses focused on a gas target, creating a plasma channel for efficient proton acceleration. Advantages include compactness due to its reliance on lasers instead of large magnets, potentially lower construction and maintenance costs, and scalability to different energy requirements. However, challenges remain. Current LWFA setups have low repetition rates, hindering continuous treatment delivery, and achieving precise beam quality might require additional techniques.

Conversely, PWFA utilizes a bunched relativistic electron beam within a cold plasma to create a wakefield for accelerating charged particles, including protons. While PWFA development has been more gradual, it offers the potential for even higher

energy gains within a more compact design than LWFA. However, challenges such as optimizing wakefield generation and achieving precise control over the acceleration process also exist with PWFA.

The potential of superconductors to create more compact and efficient accelerators is also being actively explored. The HITRIplus [24] project is funded by the European Union, exemplifies this approach by studying a novel superconducting magnet synchrotron for carbon ions alongside a compact helium ion synchrotron [18]. It demonstrates how superconductor technology can be leveraged to optimize existing synchrotron designs for size and cost reduction, making them a more viable option for hadron therapy [25].

Medical cyclotrons with superconducting magnets offer another compelling solution. Traditional cyclotrons are reliable but bulky [6]. Superconducting magnets offer significant advantages by drastically reducing cyclotrons' size and power consumption, leading to compactness, operational cost savings due to lower power usage, and a well-established and reliable technology base. However, challenges exist as well [26]. Superconducting medical cyclotrons are a relatively new technology requiring further development for widespread adoption. Additionally, the upfront cost of superconducting magnets might be higher than traditional ones, although operational cost savings can offset this. While suitable for protons, this technology might require further development for effective use with heavier ions commonly employed in hadron therapy.

The pursuit of compact and cost-effective solutions for hadron therapy accelerators necessitates exploring various avenues. LWFA, PWFA, and superconducting accelerators all hold promise for achieving these goals. As research progresses and these technologies mature, they have the potential to revolutionize cancer treatment by enabling more powerful, compact, and adaptable accelerators, ultimately leading to more effective treatment options for a wider range of patients.

2.2.3. Beam handling

Prior to treatment, ion beams require precise energy tailoring. Although cyclotrons generate a fixed high-energy beam (around 230 MeV), an "energy degrader" (adjustable graphite wedges) fine-tunes the energy to a variable range between 60 and 230 MeV. This system, known as the Energy Selection System, can make these

adjustments very rapidly (less than a second). While some beam intensity is lost during degradation, cyclotrons typically produce enough to overcome this.

Synchrotrons achieve variable beam energy through a distinct approach. By extracting the beam at specific points within its acceleration cycle, they can deliver protons in over 90 discrete energy steps, ranging from 73 MeV to 222 MeV. This translates to different depths of penetration within tissue (4 to 31 cm).

Superconducting magnets are a cornerstone of modern ion therapy systems, especially crucial for synchrotrons to handle high-energy ion beams like 430 MeV/nucleon carbon ions [24].

2.2.4. Gantry

After reaching therapeutic energies, proton beams need to be shaped and delivered with high accuracy to the target tumor within the patient. This critical step ensures the maximum dose is concentrated on the tumor while minimizing exposure to healthy tissues.

Proton beams initially have a narrow profile, making them unsuitable for treating irregularly shaped tumors or patients with varying tissue densities. To overcome this limitation, the beams require broadening in both the longitudinal and lateral directions. This process, called beam shaping, allows for tailoring the beam profile to precisely match the three-dimensional shape of the target tumor.

Two primary techniques are employed to achieve beam shaping [10]:

1. **Passively Scattered Proton Therapy (PSPT):** This method uses scattering and energy modulation of single-energy proton beams.
2. **Intensity-Modulated Proton Therapy (IMPT):** This more advanced approach utilizes magnetic scanning of narrow proton beamlets with varying energies.

IMPT offers a more sophisticated approach compared to PSPT, allowing for even greater conformity of the dose to the tumor, potentially leading to better treatment outcomes. Both techniques involve directing multiple beams from different angles to converge on the target area. This multi-directional delivery is facilitated by the gantry, a large rotating structure that houses the nozzle and the entire beam delivery system. The gantry precisely maneuvers the beam to irradiate the tumor located at the isocenter

from various angles, ensuring complete coverage while minimizing exposure to healthy tissues (Figure 2.5 [1]).
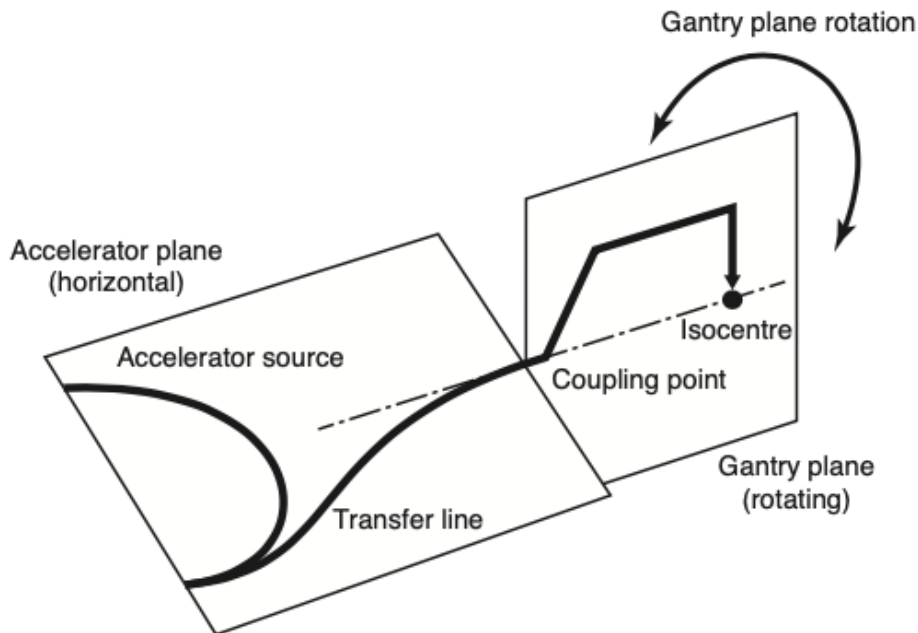
Figure 2.5. Schematic illustration of the rotation of a gantry around the patient (isocenter).

Despite their technological advancements, proton therapy gantries present a significant hurdle due to their sheer size. These intricate machines, often exceeding 7.5 meters in diameter and weighing over 100 tons (as seen in Figure 2.6 [27]), necessitate complex engineering to guarantee precise beam delivery. This translates to substantial costs throughout the entire lifecycle of these facilities, encompassing construction, operation, and maintenance.

Degrader and collimator

Momentum
slits

Isocenter

S2C2

extraction
beam line

Compact gantry (CGTR)
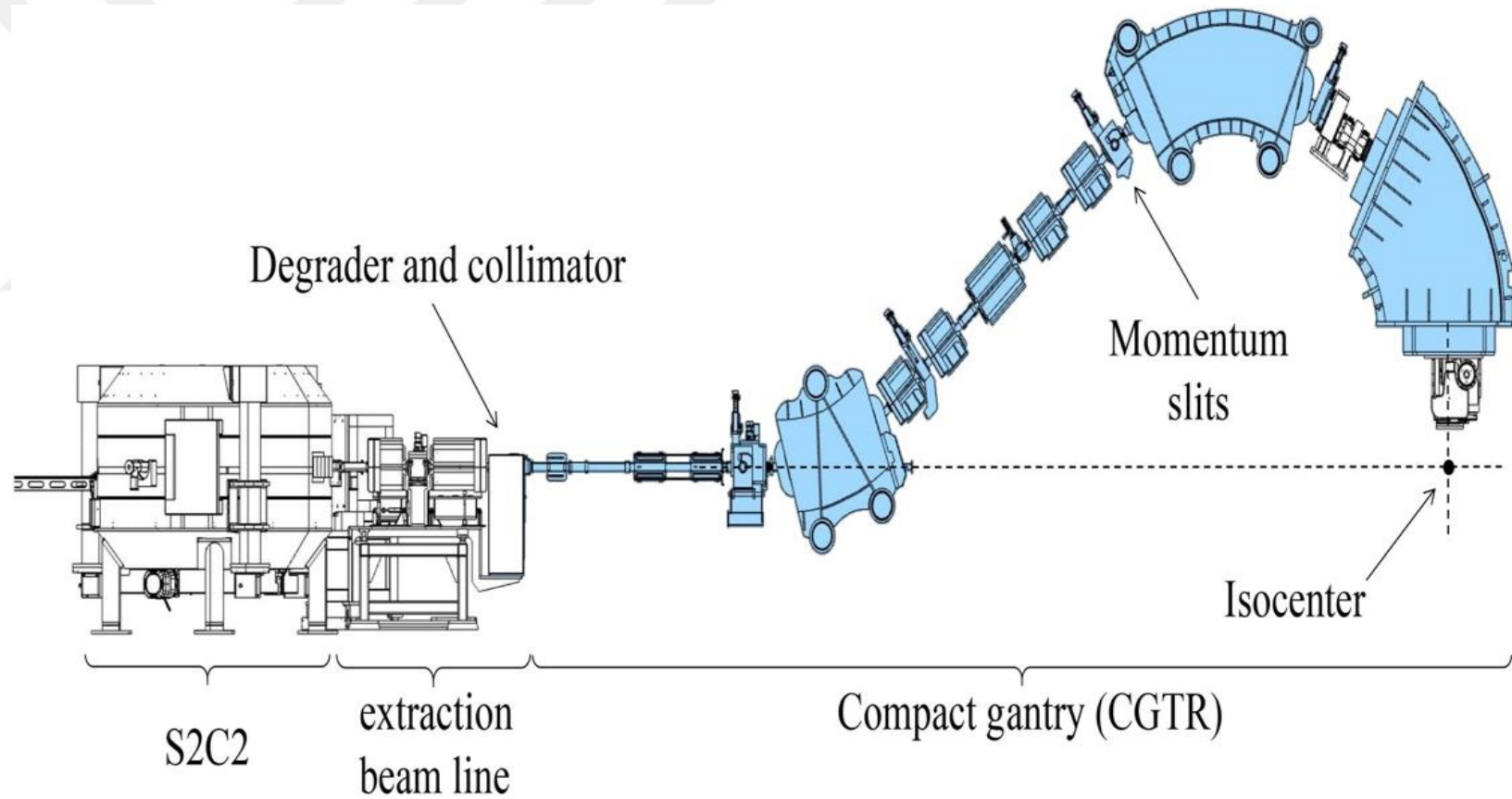
Figure 2.6. The PROTEUS-ONE proton therapy gantry (IBA) is a compact design with a ±120° rotation and 7.5 meter diameter. While smaller than some gantries, it still represents a marvel of engineering due to the complex design required for precise beam delivery.

Figure 2.7. The Heidelberg carbon-ion gantry with 25 m length and 13 m diameter.

Just like proton therapy gantries, their carbon therapy counterparts present a major challenge due to their enormous size. Unlike lighter protons, carbon ions require heavier machinery for precise control during treatment. These complex machines, like the one shown in Figure 2.7, can be massive, often exceeding 600 tons. This sheer size necessitates advanced engineering, contributing significantly to the high cost of building and operating carbon therapy facilities.

High costs are a major hurdle for the widespread use of hadron therapy. Building and running these facilities require a hefty investment due to the advanced technology involved. Superconducting magnets offer a bright spot in reducing these costs. These magnets are essential for steering and focusing the high-energy particle beams used in treatment. By enabling smaller designs for the machines that accelerate and deliver the particles (accelerators and gantries) [28], [29], superconductors help shrink the physical footprint of the entire facility, leading to lower overall costs.

Making hadron therapy more accessible to patients requires developing compact and efficient facilities [30]. Superconducting technology plays a key role in achieving this

goal. For example, Varian Medical Systems is researching different superconducting technologies to design smaller cyclotrons and gantries specifically for proton therapy [31].

Superconducting gantries have been around for over a decade, and advancements continue. Let's look at two specific examples that illustrate the impact of superconductors on reducing treatment facility size and cost:

1. Mevion S250: Compact design for proton therapy

The Mevion S250 therapy system is a game-changer in terms of size and efficiency for proton therapy. It integrates a powerful superconducting synchrocyclotron (22 tons, Nb_3Sn coils, 8.5T) directly onto a rotating gantry (see Figure 2.8). This innovative design eliminates the need for a separate accelerator and transfer line, resulting in a remarkably compact footprint of 140-180 m^2 (estimated gantry radius of 4.2 meters). This showcases the potential of superconductors in creating smaller and more efficient hadron therapy systems.
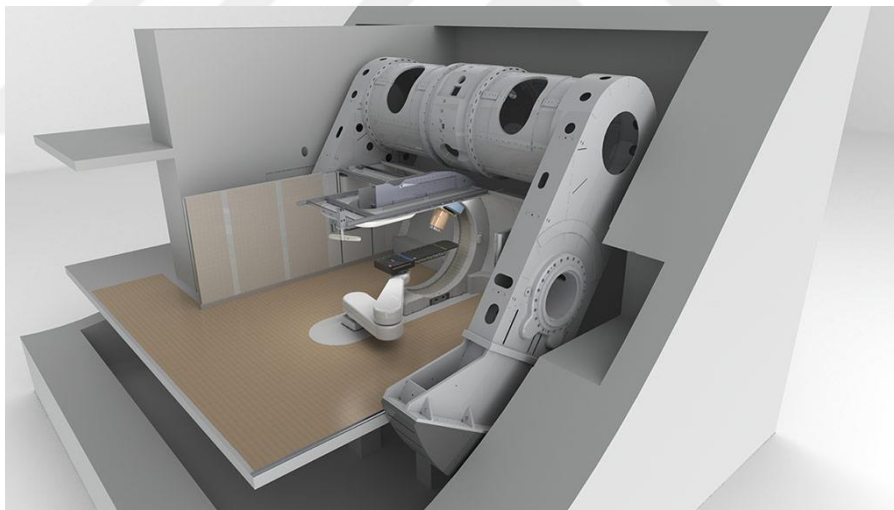
Figure 2.8. Mevion S250: This innovative design directly integrates a powerful superconducting synchrocyclotron onto a rotating gantry, eliminating the need for separate equipment and resulting in a remarkably compact proton therapy system.

3. NIRS Superconducting Gantry: Compact design for carbon ion therapy

The National Institute of Radiological Sciences (NIRS) in Japan has developed a groundbreaking carbon ion therapy system with a compact design (around 300 tons, 5.5 meters wide and 13 meters long). This is achieved through powerful superconducting magnets (almost 3 Tesla peak and a gradient of 9.3 Tesla per meter)

that eliminate the need for larger components (see Figure 2.9). This innovative design allows for a full 360-degree rotation of the gantry for flexible treatment angles and a treatment area of 200 mm² [30-32].

Researchers are pushing the boundaries by exploring even stronger magnets (5 Tesla peak and 15 Tesla per meter gradient) for smaller gantry designs. These stronger magnets have the potential to shrink the gantry to a size comparable to proton therapy systems (around 4 meters wide and 5 meters long).
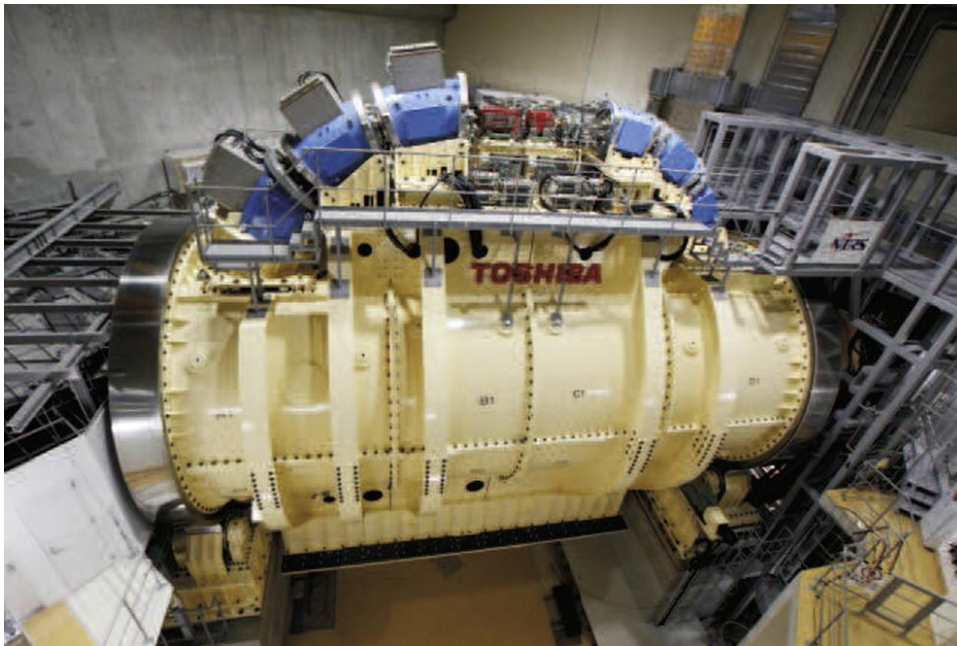
Figure 2.9. Compact design: NIRS superconducting gantry.

The field of superconducting gantries continues to evolve with innovative solutions like the toroidal gantry (GaToroid) concept [33]. GaToroid aims to revolutionize beam delivery using a toroidal (doughnut-shaped) magnetic field generated by lightweight superconducting magnets [34], [35]. This design has the potential to be even more compact and cost-effective than traditional gantries, potentially making hadron therapy even more accessible to a broader range of patients.

The key innovation lies in GaToroid's lightweight, superconducting design. Unlike traditional gantries that require complex and expensive mechanical rotation, GaToroid encircles the patient, enabling treatment from various angles without the need for movement. This significantly reduces costs and complexity, potentially improving patient treatment comfort.

2.3. GaToroid

Traditional hadron therapy gantries employ rotating mechanisms for beam angle adjustment, significantly increasing their complexity, size, and weight. Unlike accelerator facilities that scale their radius for higher energies, gantries face a crucial limitation: size. This restricts the ability to deliver beams from multiple angles, a vital factor for treatment efficiency. Superconducting ion gantries offer a Cutting-edge solution. By leveraging superconductors, they achieve a significant size reduction while simultaneously boosting the available magnetic field flux. This design overcomes the size constraint, enabling efficient and precise beam delivery.

Recognizing the limitations of conventional rotating gantries, Bottura et al. proposed an innovative concept for hadron therapy: a toroidal gantry, or GaToroid operateing in a steady state and eliminas the need for complex rotation mechanisms. The gantry utilizes high-field superconducting magnets, exceeding the capabilities of traditional iron-based magnets, to achieve the necessary magnetic field configuration [34]. This combination of a toroidal design with superconducting technology, holds significant promise for dramatically reducing the size and mass of gantries.

At its core, the GaToroid concept consists of two key components, as illustrated in Figure 2.10 [33]. The first is a vector magnet positioned where the beam enters from the accelerator. This magnet provides a "kick" to the beam, with the strength dependent on both the beam energy and the desired delivery direction. The second component is one or more co-axial toroidal magnets. These donut-shaped magnets bend the beam through a combination of their shape and the variation of the magnetic field within them. The patient is then positioned along the axis of these toroidal magnets, allowing for precise beam delivery.
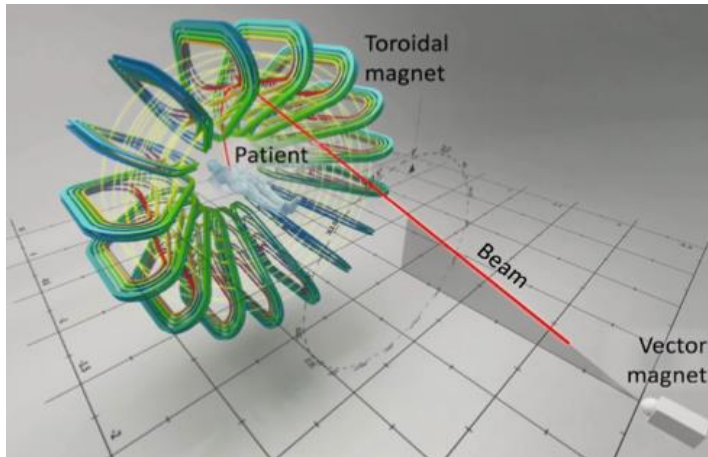
Figure 2.10. Schematic representation of GaToroid superconducting torus, beam, vector magnet, and patient positioning (courtesy of Daniel Dominguez, CERN design and Visual Identity Service).

The gantry design began with defining the ideal coil shape. This initial concept served as the foundation for constructing real-world coils. The design process then involved meticulously segmenting these ideal coils into 16 discrete sectors, each with 5 distinct grades [33], [36]. The coil geometry was parameterized for numerical optimization, accommodating feasible bending radii and simplified regions dictated by specific equations. The spacing among grades was fine-tuned through optimization to achieve optimal beam bending properties while minimizing the peak field on the winding. The resulting geometry of the complete torus of 16 coils, along with the support structure concept, and a single coil is visually illustrated in Figure 2.10 and Figure 2.11, respectively.
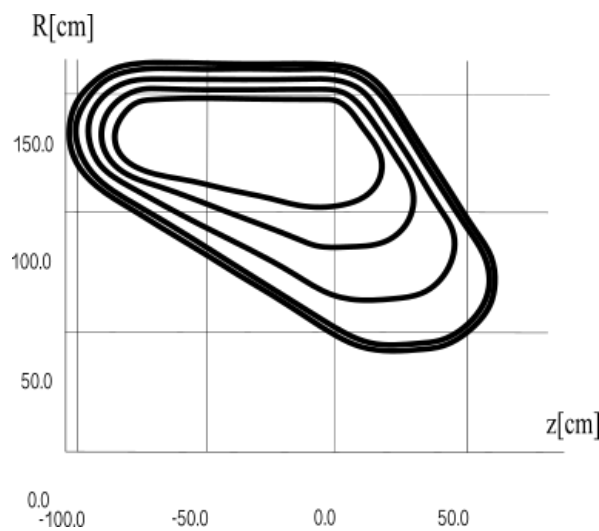
Figure 2.11. One coil optimized for GaToroid.

36

2.4. Simulation Tools

Hadron therapy relies heavily on accurate predictions of radiation dose distribution within the patient's body. This task is complex because different organs possess varying densities and atomic compositions, making precise dose calculations challenging. Tailored algorithms, such as the pencil beam algorithm and Monte Carlo (MC) simulations, address this challenge.

While offering the most accurate dose predictions, MC simulations require significant computational power, translating to longer processing times. Despite this drawback, MC simulations remain the gold standard in radiotherapy. They are invaluable tools for evaluating physical properties that are either impractical or difficult to measure directly. They are significant tools for:

- **Radiotherapy device design**: MC simulations allow for optimizing and testing new radiotherapy devices before physical prototypes are built.

- **Treatment planning:** These simulations help doctors create precise treatment plans by accurately predicting how radiation interacts with different tissues within the patient.

- **Understanding radiation therapy intricacies:** MC simulations provide valuable insights into the complex physical processes that occur during radiation therapy, leading to a deeper understanding of treatment effectiveness and potential side effects.

A variety of simulation tools, including FLUKA, GEANT4, MCNPX, SHIELD/SHIELD-HIT, and PHITS, to accurately model and analyze particle interactions.

MC simulations are indispensable for hadron therapy treatment planning and medical physics research [21]. In this study, FLUKA (FLUktuierende KAskade) version 4.4.0, simulation pakage has been used to model GaToroid system. FLUKA comprehensively models particle interactions and energy deposition within biological tissues[37]. This capability facilitates the optimization of treatment parameters and the design of safer and more efficacious therapy protocols.

Developed at CERN by J. Ranft in the 1960s, FLUKA's origins lie in MC programs designed for shielding calculations, induced radioactivity estimations, and dose absorption prediction in high-energy proton accelerators [38]. Initially, it functioned

as an analog code simulating particle cascades in cylindrical elemental material blocks, calculating spatial distributions of nuclear reactions and energy deposition densities. User input was provided via formatted control and data cards, a feature still utilized [37].

FLUKA simulates particle transport and interactions across a vast energy spectrum, ranging from a few keV to cosmic ray energies [38-40]. Its foundation in fundamental physics research, exemplified by institutions like CERN, has made it instrumental in studying beam-machine interactions and radiation damage. FLUKA offers precise predictions for both electromagnetic and nuclear interactions [41]. Beyond these fundamental applications, NASA has leveraged FLUKA's capabilities to analyze radiation exposure for astronauts on space missions, demonstrating its adaptability to real-world scenarios.

Furthermore, FLUKA has significantly impacted advanced cancer treatment planning, particularly at the Heidelberg Ion Beam Therapy Center (HIT) in Germany. Here, it supports treatment planning for patients undergoing ion beam radiotherapy by providing accurate models for data generation and access to commercial software.

FLUKA's applications extend to crucial areas like shielding design, where it plays a vital role in crafting effective radiation barriers [42], [43], [44]. Additionally, it is extensively employed in detector design, aiding in creating and optimizing detectors for various scientific and medical purposes.

In conclusion, FLUKA's strength lies in its ability to model complex geometries, making it ideal for GaToroid's toroidal gantry. This allows for optimized modeling of proton beam behavior within the system, ultimately leading to improved treatment effectiveness for proton therapy delivered by GaToroid.

3. MAGNETIC FIELD IN TOROIDAL COORDINATES

3.1. Introduction

This chapter explores the magnetic field within a novel proton therapy gantry design, the GaToroid. We leverage the power of toroidal coordinates, which naturally align with GaToroid's inherent toroidal symmetry [45], for efficient and accurate calculations.

The fundamental principles of toroidal coordinates are established in this section. These coordinates are crucial for unraveling the complexities of the magnetic field structure within toroidal devices like GaToroid. Their unique properties render them indispensable for precisely representing the spatial variations and configurations of the magnetic field within GaToroid.

The discussion commences with a comprehensive introduction to toroidal coordinates, followed by solutions of Laplace's equation within this framework. Established methods for determining toroidal harmonics and relevant terminology are reviewed. Next, transforming the magnetic field obtained through these harmonics into Cartesian coordinates is explained, facilitating further analysis in a more familiar coordinate system.

The chapter's conclusion will establish a foundation for the subsequent chapter. There, the task of finding toroidal harmonics and applying them, with the necessary transformations, within GaToroid using the FLUKA Monte Carlo code will be explored. This paves the way for a deeper understanding of the magnetic field's behavior and its implications for GaToroid's functionality.

3.2. Toroidal Coordinate

Toroidal coordinates, denoted by (ξ, η, ϕ), are a specialized coordinate system used to describe the position of a point in space relative to a toroid (donut shape). Unlike the familiar Cartesian (x, y, z) or spherical (r, θ, φ) coordinates, toroidal coordinates

are particularly useful for solving problems involving symmetrical toroidal shapes, such as the magnetic field within a toroidal confinement device used in fusion research.

3.2.1. Torus

The key concept behind toroidal coordinates lies in their relationship to bipolar coordinates. Strictly speaking, a two-dimensional bipolar coordinate system (ξ, η) already exists (as shown in Figure 3.1).
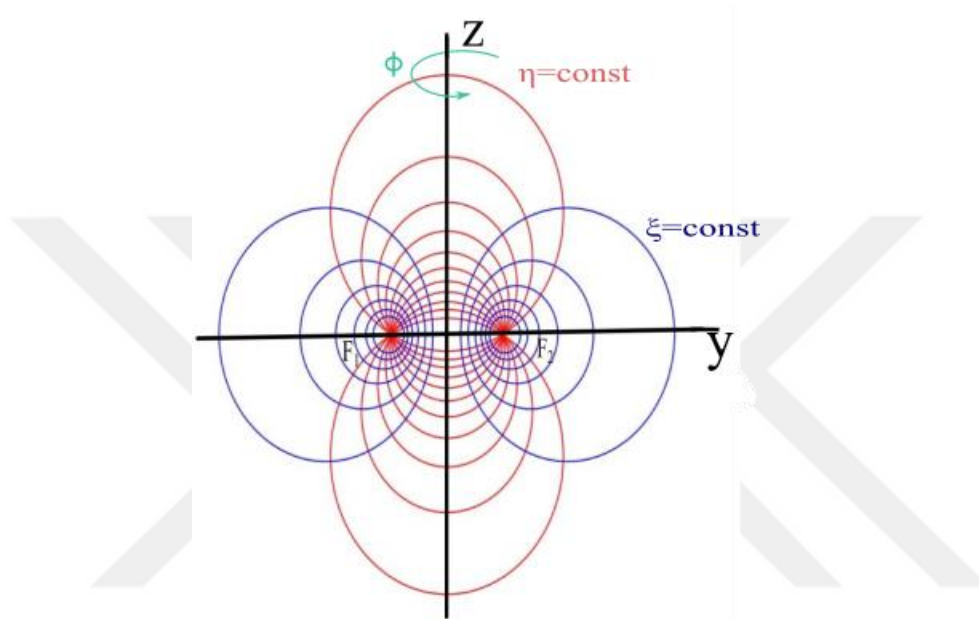
Figure 3.1. Bipolar coordinates.

A two-dimensional bipolar coordinate system (ξ, η) is first conceived. In this system, points are defined by their distance from two fixed points (foci F_1 and F_2). This two-dimensional bipolar coordinate system is then rotated around the axis, separating the two foci (Z). By performing this rotation, a three-dimensional toroidal coordinate system (ξ, η, ϕ) is generated. Essentially, this rotation creates the familiar donut shape of a torus (Figure 3.2).
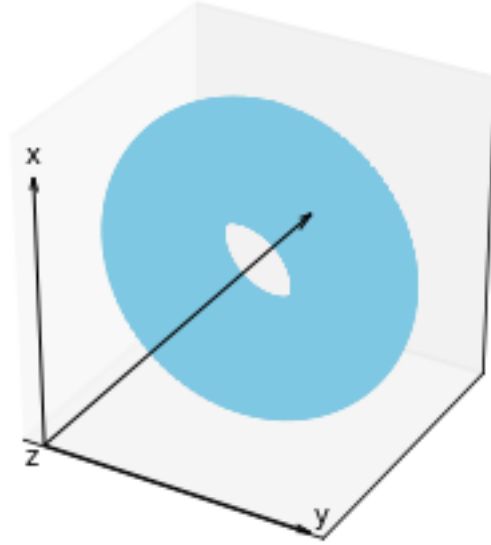
Figure 3.2. Toroidal coordinate system: a torus.

The defining feature of toroidal coordinates is the reference surface they describe, which is a torus. equations 3.1a, 3.1b, and 3.1c represent the mathematical definition of toroidal coordinates in terms of more fundamental coordinates (often Cartesian coordinates). Toroidal coordinates (ξ, η, ϕ) are given as:

$$x = \frac{a \sinh \xi \cos \phi}{k} \tag{3.1a}$$

$$y = \frac{a \sinh \xi \sin \phi}{k} \tag{3.1b}$$

$$z = \frac{a \sin \eta}{k} \tag{3.1c}$$

where $k = \cosh \xi - \cos \eta$, $\xi \in [0, 2\pi)$, $\eta \in [0, \infty)$, $\phi \in [0, 2\pi)$.

For a more intuitive understanding, let's focus on the geometric properties of the torus itself. The surface of $\xi = $ constant makes a torus with the equation

$$z^2 + \left(\sqrt{x^2 + y^2} - a \coth \xi\right)^2 = \frac{a^2}{\sinh^2 \xi} \tag{3.2}$$

Equation 3.2 involves two key parameters:

- **Major Radius** ($R = a/\tanh \xi$): This represents the radius of the imaginary circle that forms the "centerline" of the torus (think of the hole in the donut).

- **Minor Radius** ($r = a/\sinh\xi$): This represents the radius of the cross-section of the torus itself (the thickness of the donut).

Figure 3.3 provides a visual representation of a torus [46]. Imagine a small circle with radius r rotating around the z-axis. As this circle completes a full rotation, it sweeps out a toroidal surface. The distance between the center of the rotating circle and the z-axis determines the major radius of the resulting torus.
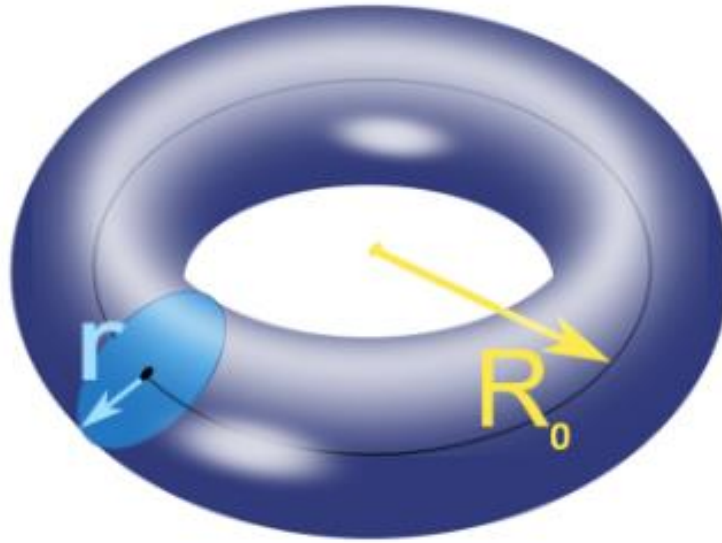
Figure 3.3. Representation of a generic torus's minor (light blue) and major (yellow) radius.

With the concept of toroidal coordinates and their connection to the toroidal shape established, the conversion process from the familiar Cartesian coordinate system (*x, y, z*) to toroidal coordinates will now be explored. This conversion process holds particular value for simulations involving toroidal shapes.

$$\xi = \ln\frac{d_1}{d_2} \tag{3.3a}$$

$$\cos\eta = -\frac{4a^2 - d_1^2 - d_2^2}{2d_1d_2} \tag{3.3b}$$

$$\tan\phi = \frac{y}{x} \tag{3.3c}$$

where $d_1 = \sqrt{(\rho + a)^2 + z^2}$ and $d_2 = \sqrt{(\rho - a)^2 + z^2}$ (see Figure 3.4) are the distance of any point like P at torus surface from foci F_1 and F_2 located at $(-a, 0)$ and $(a, 0)$ respectively and $\rho = \sqrt{x^2 + y^2}$.
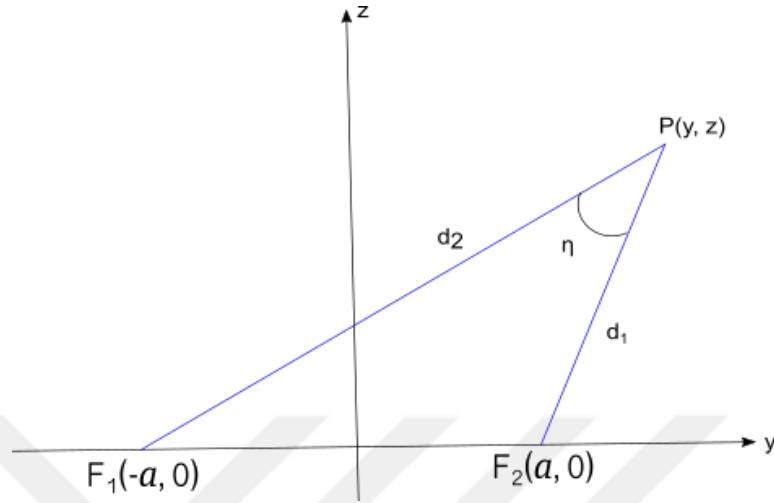
Figure 3.4. Representation of the parameters defining bipolar coordinates.

3.2.2. Toroidal grid

To determine the observable points in toroidal coordinates, the concept of a grid can be employed as the parametric equations[46]:

$$x = (R_0 + r \cos \theta) \sin \varphi \qquad (3.4a)$$

$$y = (R_0 + r \cos \theta) \cos \varphi \qquad (3.4b)$$

$$z = r \sin \theta \qquad (3.4c)$$

where r and R_0 is minor and major radius θ is the poloidal angle and φ is the toroidal angle (see Figure 3.5).
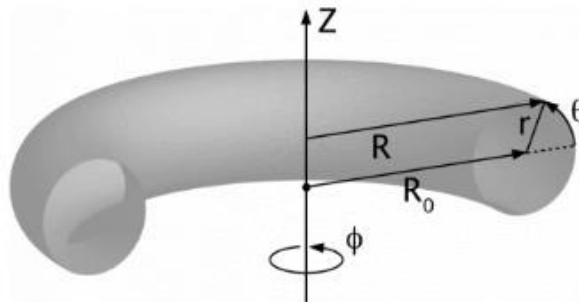
Figure 3.5. Representation of a toroidal geometry in cylindrical coordinates.

These reference grids are essential for identifying the scalar potentials, which will be discussed in subsequent sections. The grid method allows for a systematic approach to mapping toroidal coordinates, facilitating the accurate determination of scalar potentials necessary for solving Laplace's equation and analyzing magnetic fields within toroidal systems. Establishing these reference points is crucial for ensuring precision in the calculations and transformations that follow in our study. Figure 3.6 illustrates an example of this grid within a toroid composed of 16 coils.
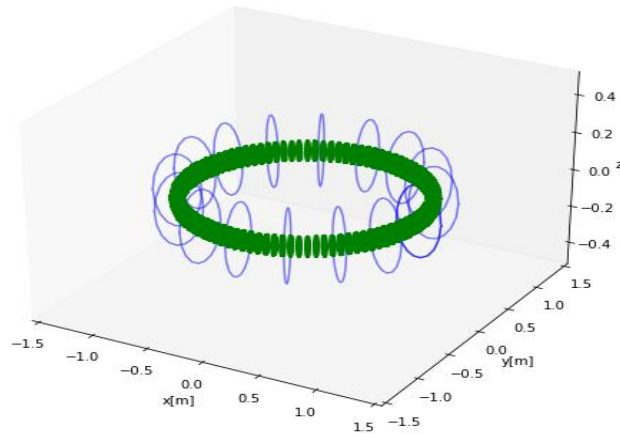
Figure 3.6. Toroidal grid (green) within a 16-coil toroid (blue).

3.3. Toroidal Harmonics

In order to analyze the magnetic field within a vacuum-filled toroid generated by current-carrying coils, Laplace's equation, $\nabla^2 \psi = 0$, is employed. Here, ψ is defined as a scalar potential, with its gradient representing the magnetic field, *H*, of the toroid.

3.3.1. General solution

The solution of the Laplace equation in toroidal coordinates results in toroidal harmonics. Toroidal-harmonic solutions of Laplace's equation are currently receiving widespread attention due to their versatility and effectiveness in modeling complex magnetic fields and other physical phenomena. They are extensively utilized in understanding magnetic confinement in fusion reactors like tokamak. Beyond fusion research, toroidal harmonics find applications in plasma physics [47], astrophysics [48], and electromagnetism.

Following a procedure outlined in reference [46]. for extracting toroidal harmonics, a solution utilizing the R-separation method as detailed in [30], [31] yields:

$$
\begin{aligned}
\psi(\xi, \eta, \phi) = \ & M_{00}^{\phi}\phi \\
& + k^{\frac{1}{2}} \sum_{m=1}^{M} \sum_{n=0}^{N} Q_{m-\frac{1}{2}}^{n}(\cosh(\xi)) \\
& \times \big[M_{m,n}^{cc} \cos(n\phi)\cos(m\eta) \\
& + M_{m,n}^{cs} \cos(n\phi)\sin(m\eta) \\
& + M_{m,n}^{sc} \sin(n\phi)\cos(m\eta) + M_{m,n}^{ss} \sin(n\phi)\sin(m\eta) \big]
\end{aligned}
\tag{3.5}
$$

where (ξ, η, ϕ) represent the toroidal coordinates, $k = \cosh\xi - \cos\eta$, the multipolar coefficients M_{ij} are associated with the specific harmonic mode $(n,\ m)$. These coefficients encode information about the field strength and symmetry, and term $Q_{m-1/2}^{n}$ is the half-integer Legendre polynomials of the second kind. The multipole moments found in the scalar potential expression can be directly interpreted as the field components of the $m = 1$ for dipole, $m = 2$ for quadrupole, $m = 3$ for sextupole, and so on. The variable n specifies the periodic intervals at which the coils are located. For N_T coils, $n = 0, N_T, 2N_T, \ldots, N$.

The term M_{00}^{ϕ} is called the ideal contribution, resulting from homogenous current distribution on a toroidal surface. This contribution does not depend on the coil geometry; it can be demonstrated that

$$
M_{00}^{\phi} = \frac{\mu_0 NI}{2\pi}
\tag{3.6}
$$

where $\mu_0 = 4\pi \times 10^{-7}$ N/A^2 is the permeability of free space, N is the number of coils of the magnetic configuration and I the current flowing in each coil.

Although the solution of Laplace's equation in toroidal coordinates is expressed as equation 3.5, the presence of the half-integer Legendre term complicates the determination of polynomial constants, requiring numerical methods. To address this complexity, as indicated on the left side of equation 3.5, accurately determining the corresponding scalar potential at each point inside the toroid is crucial. This allows the multipolar coefficients on the right side to be precisely obtained through fitting

methods. Therefore, the first step in determining the multipole constants is to acquire the scalar potential at the observed points or grid references within the toroid.

3.3.2. Finding scalar potential

The method used to determine the scalar potential (ψ) relies on the scalar field model generated by the current (I) of all loops at the observed point (r), considering the solid angle (Ω) relative to it [51].

$$\psi(\mathbf{r}) = \frac{I}{4\pi}\Omega(\boldsymbol{r}) \tag{3.7}$$

This approach utilizes the triangular plane approximation for solid angle calculations [52]. Using equation 3.7, the scalar potential is calculated for a fixed radial coordinate $\xi = \xi_0$ and for L values of the poloidal angle η and S values of the toroidal angle ϕ.

3.3.3. Fitting method

To isolate specific scalar potential values, a particular value, ϕ_S, can be assigned to ϕ. Consequently, At fixed radial coordinate $\xi = \xi_0$ equation 3.5 can be rewritten as follows:

$$\begin{aligned}
\psi(\xi_0, \eta, \phi_s) = \ & M_{00}^{\phi}\phi_s \\
& + \sqrt{\cosh(\xi_0) - \cos(\eta)} \\
& \times \sum_{m=1}^{M} (A_m(\xi_0, \phi_s)\cos(m\eta) + B_m(\xi_0, \phi_s)\sin(m\eta))
\end{aligned} \tag{3.8}$$

where $A_m(\xi_0, \phi_s)$ and $B_m(\xi_0, \phi_s)$ are two constant values defined as:

$$A_m(\xi_0, \phi_s) = \sum_{n=0}^{N} Q_{m-\frac{1}{2}}^{n}(\cosh(\xi_0))\left[M_{m,n}^{cc}\cos(n\phi_s) + M_{m,n}^{sc}\sin(n\phi_s)\right] \tag{3.9a}$$

$$B_m(\xi_0, \phi_s) = \sum_{n=0}^{N} Q_{m-\frac{1}{2}}^{n}(\cosh(\xi_0))\left[M_{m,n}^{cs}\cos(n\phi_s) + M_{m,n}^{ss}\sin(n\phi_s)\right] \tag{3.9b}$$

For L scalar fields corresponding to the same toroidal angle, Equation 3.8 can be resolved using a fitting method to determine the constants M_{00}^{ϕ}, A_m and B_m. It is important to note, as indicated in the first term of equation 3.8, the scalar field is

directly related to ϕ_s, and varying ϕ_s yields different sets of solutions for menthioned constants, especially M_{00}^{ϕ}. Consequently, the following method sugests the optimal value among these solutions.

3.3.3.1. Root mean square error and R^2

The root mean square error (RMSE)[53] is a quantitative metric for assessing the discrepancy between a statistical model's predicted values and the actual observed values in a dataset. Mathematically, it is expressed as the standard deviation of the residuals, which represent the individual differences between observed data points and the values predicted by the fitted regression line.

The RMSE value reflects the spread of these residuals, essentially indicating how closely the observed data points cluster around the predicted values. As the data points align more closely with the regression line, the model's error diminishes, leading to a lower RMSE. Conversely, a higher RMSE signifies a greater disparity between observed and predicted values, suggesting a larger model error and potentially less precise predictions. Therefore, a model with a lower RMSE value is generally considered to fit the data more effectively and generate more accurate predictions.

The formula for RMSE is:

$$RMSE = \sqrt{\frac{1}{M} \sum_{i=1}^{M} (y_i - \hat{y}_i)^2} \tag{3.10}$$

where:

- M is the number of observations.
- y_i represents the actual value.
- $\hat{y}_i$ represents the predicted value.

Another useful concept for indicating the goodness of fit of a model is the R^2 (R-squared) statistic, also known as the coefficient of determination:

$$R^2 = 1 - \frac{\sum_{i=1}^{M}(y_i - \hat{y}_i)^2}{\sum_{i=1}^{M}(y_i - \bar{y})^2} \tag{3.11}$$

where $\bar{y}$ is the mean of the actual values, and the other parameters are as previously defined. The R^2 value ranges between 0 and 1:

- An $R^2 = 1$, indicates that the model perfectly fits the data.
- An $R^2 = 0$, indicates that the model does not explain any of the variability of the response data around its mean.

Following the application of RMSE and R^2 analysis, the constant value of M_{00}^{ϕ}, is established. With this constant held fixed, a range of S values for the toroidal angle ϕ are then applied to equation 3.8. Utilizing a fitting method, corresponding S values for A_m and B_m are subsequently determined. These processes are referred to as Fitting 2A and Fitting 2B, respectively [46].

3.3.3.2. Fitting 2A

Values of A_m are evaluated at $\xi = \xi_0$ for S equidistant angles ϕ in the Fitting equation 3.12, which is written with the coordinate ϕ variable rather than fixed. The output consists of the coefficients $M_{m,n}^{cc}$ and $M_{m,n}^{sc}$.

$$A_m(\xi_0, \phi) = \sum_{n=0}^{N} Q_{m-\frac{1}{2}}^n(\cosh(\xi_0)) \left[M_{m,n}^{cc} \cos(n\phi) + M_{m,n}^{sc} \sin(n\phi) \right] \tag{3.12}$$

3.3.3.3. Fitting 2B

Values of B_m are evaluated at $\xi = \xi_0$ for S equidistant angles ϕ in the Fitting equation 3.13, which is written with the coordinate ϕ variable rather than fixed. The output consists of the coefficients $M_{m,n}^{cs}$ and $M_{m,n}^{ss}$.

$$B_m(\xi_0, \phi) = \sum_{n=0}^{N} Q_{m-\frac{1}{2}}^n(\cosh(\xi_0)) \left[M_{m,n}^{cs} \cos(n\phi) + M_{m,n}^{ss} \sin(n\phi) \right] \tag{3.13}$$

Upon completing the fitting procedures, the values of each coefficient used in the multipolar expansion of the scalar potential are determined. These coefficients can then be substituted into the expressions for the magnetic field components in the next section.

3.4. Magnetic Field

The magnetic field components are determined by taking the gradient of the scalar potential expression in toroidal coordinates[46].

$$B_\xi(\xi,\eta,\phi) = \frac{k^{\frac{3}{2}}}{a} \sum_{m=1}^{M} \sum_{n=0}^{N} \left[M_{m,n}^{cc} \cos(n\phi) \cos(m\eta) \right.$$

$$+ M_{m,n}^{cs} \cos(n\phi) \sin(m\eta) + M_{m,n}^{sc} \sin(n\phi) \cos(m\eta) \tag{3.14a}$$

$$\left. + M_{m,n}^{ss} \cos(n\phi) \sin(m\eta) \right]$$

$$\times \left\{ \frac{1}{2} k^{-1} \sinh(\xi) \, Q_{m-\frac{1}{2}}^{n}(\cosh(\xi)) + \frac{\partial}{\partial x} Q_{m-\frac{1}{2}}^{n}(\cosh(\xi)) \right\}$$

$$B_\eta(\xi,\eta,\phi) = \frac{k^{\frac{3}{2}}}{a} \sum_{m=1}^{M} \sum_{n=0}^{N} Q_{m-\frac{1}{2}}^{n}(\cosh(\xi)) \left[\frac{1}{2} \sin(\eta) \, k^{-1} \right.$$

$$\times \left(M_{m,n}^{cc} \cos(n\phi) \cos(m\eta) + M_{m,n}^{cs} \cos(n\phi) \sin(m\eta) \right.$$

$$\left. + M_{m,n}^{sc} \sin(n\phi) \cos(m\eta) + M_{m,n}^{ss} \cos(n\phi) \sin(m\eta) \right) \tag{3.14b}$$

$$+ m \left(-M_{m,n}^{cc} \cos(n\phi) \sin(m\eta) + M_{m,n}^{cs} \cos(n\phi) \cos(m\eta) \right.$$

$$\left.\left. - M_{m,n}^{sc} \sin(n\phi) \sin(m\eta) + M_{m,n}^{ss} \sin(n\phi) \cos(m\eta) \right) \right]$$

$$B_\phi(\xi,\eta,\phi) = \frac{k M_{00}^{\phi}}{a \sinh(\xi)}$$

$$+ \frac{k^{\frac{3}{2}}}{a \sinh(\xi)} \sum_{m=1}^{M} \sum_{n=0}^{N} n Q_{m-\frac{1}{2}}^{n}(\cosh(\xi)) \tag{3.14c}$$

$$\times \left[-M_{m,n}^{cc} \sin(n\phi) \cos(m\eta) - M_{m,n}^{cs} \sin(n\phi) \sin(m\eta) \right.$$

$$\left. + M_{m,n}^{sc} \cos(n\phi) \cos(m\eta) + M_{m,n}^{ss} \cos(n\phi) \sin(m\eta) \right]$$

According to relation 3.14c, understanding the significance of the dominant term, M_{00}^{ϕ}, is crucial. It underscores the importance of accurately determining the multipole coefficients and M_{00}^{ϕ} to gauge their impact on the magnetic field components. Therefore, devising a precise procedure to ascertain their values becomes imperative, as it directly influences the behavior and characteristics of the magnetic field.

A critical step in describing the magnetic field within FLUKA simulations involves the conversion between Cartesian and toroidal coordinate systems. Equations 3.15 determine these relationships [46]:

$$B_x = \frac{(1 - \cosh\xi\cos\eta)\cos\phi}{k}B_\xi - \frac{\sinh\xi\sin\eta\cos\phi}{k}B_\eta - \sin\phi\,B_\phi \qquad (3.15a)$$

$$B_y = \frac{(1 - \cosh\xi\cos\eta)\sin\phi}{k}B_\xi - \frac{\sinh\xi\sin\eta\sin\phi}{k}B_\eta - \cos\phi\,B_\phi \qquad (3.15b)$$

$$B_z = \frac{-\cosh\xi\cos\eta}{k}B_\xi - \frac{(\sinh\xi\sin\eta - 1)}{k}B_\eta \qquad (3.15c)$$

4. MATERIALS AND METHODS

This chapter outlines the comprehensive materials and methods employed in the study, focusing on the simulation of GaToroid's influence on proton beam dynamics using the FLUKA MC code. The GaToroid is a novel magnetic device designed to optimize proton beam delivery in proton therapy, providing precise control over the beam's trajectory and intensity.

The following sections detail the geometric design of GaToroid, the configuration of the proton beam source, the implementation of the magnetic field, and the procedural steps for running the FLUKA simulations. Each component is crucial for understanding the overall methodology and ensuring the accuracy and reliability of the simulation results.

4.1. GaToroid Properties

Building upon the work presented in Reference [36], the study investigated two optimized solutions for GaToroid. These solutions are distinguished by their respective engineering current densities within the cable. This variation reflects the utilization of alternative superconducting technologies and quench protection systems. Engineering current density (J_{en}) represents the current carried by each grade divided by its cross-sectional area, considering both the superconductor and stabilizer materials.

Based on the two proposed solutions with current densities of 100 A/mm² and 500 A/mm², the solution with a current density of 500 A/mm² was selected for further simulation using FLUKA. This selection was made due to considerations of practicality. The detailed specifications of the chosen solution can be found in Tables 4.1 and 4.2.

A thorough explanation of both solutions is available in Reference [36] for a more comprehensive understanding. It is important to acknowledge that selecting either solution is expected to yield comparable MC simulation performance. The primary differentiating factors reside in the engineering structure and, consequently, the final costs of constructing the constituent superconductors.

Table 4.1. GaToroid each coil parameter for J_{en}=500 A/mm².

Parameter	Unit	
Number of grades		5
Length	[m]	1.8
Height	[m]	1.2
Thickness	[m]	0.05

Table 4.2. GaToroid parameter for J_{en}=500 A/mm².

Parameter	Unit	
Number of coils		16
Bore Radius	[m]	0.4
External Diameter	[m]	3.3
Torus Length	[m]	1.8
Vector Magnet Position	[m]	3.6

For the purpose of simulating the performance of GaToroid in proton therapy using FLUKA, this study focuses solely on the dimensions and shapes of the optimized coils as presented in Table 4.1. This emphasis on geometry is necessitated by the requirement for an accurate representation of GaToroid within the simulation environment.

To achieve the objective of simulating GaToroid geometry in FLUKA, Figure 4.1 presents the initial coil shape. This initial shape is the foundation for deriving the final GaToroid geometry, which is subsequently presented in Figure 4.2 [36].
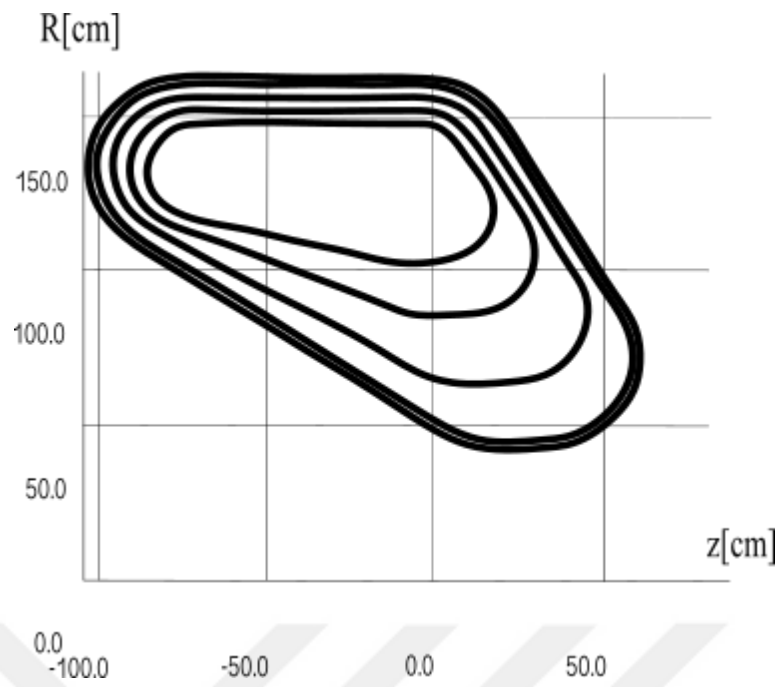
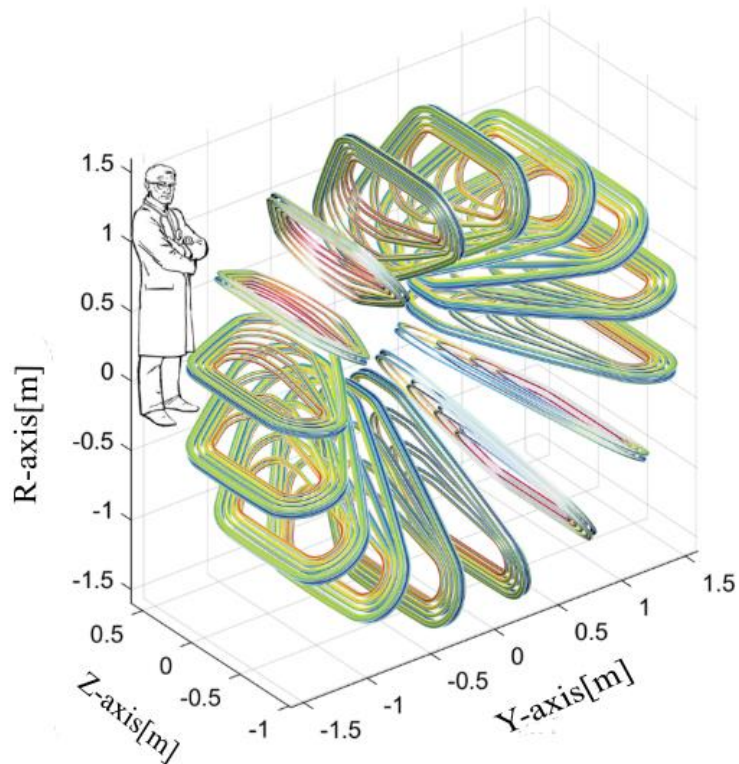**Figure 4.1.** Optimized coil dimension.

Figure 4.2. Final GaToroid geometry, a standardized human body diagram is a visual reference for scale [36].

4.2. FLUKA Code and Simulation Setup

4.2.1. Flair

FLUKA simulations for the toroidal gantry system were facilitated by Flair (version 3.3-1), a graphical user interface (GUI) for the FLUKA code [54]. While not all aspects of the simulation workflow are directly handled by Flair, it significantly enhances efficiency and accuracy in several key areas.

- **Geometry Definition:** Flair's visual interface streamlines the creation of complex geometries, essential for accurately representing the toroidal gantry's components (coils, vacuum environments, treatment isocenter).

- **Material Selection:** The built-in material database simplifies the selection of appropriate materials for gantry environments and phantom models.

- **Input File Generation and Error Checking:** The code editor with syntax highlighting facilitates the creation of error-free input files, ensuring an accurate representation of the geometry, material properties, source beam definition, scoring and primary particles within the simulations.

- **Job Management and Monitoring:** Flair expedites job management through functionalities for building executables, debugging the geometry setup, beam tracking, and monitoring the progress of multiple simulations.

- **Post-Processing Potential:** While post-processing is not directly performed within Flair, its functionalities can indirectly aid this stage by providing well-organized output files for further analysis and visualization.

Overall, Flair's user-friendly interface and emphasis on error-free input file creation significantly contributed to the efficiency and accuracy of our FLUKA simulations, version 4.4.0, for the toroidal gantry system. A visual representation of the Flair is provided in Figure 4.3.
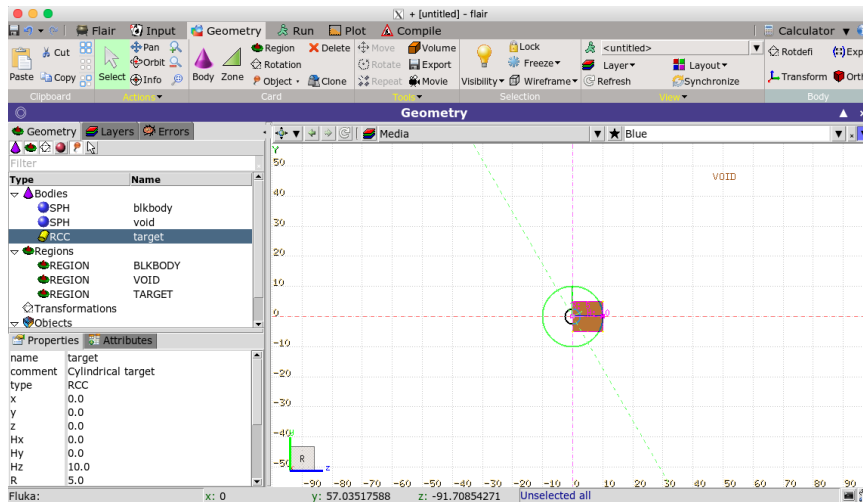
Figure 4.3. Flair: a graphical user interface (version 3.3-1).

4.2.2. Geometry design

The geometric configuration of GaToroid was defined based on a prototype model suggested by a group of CERN researchers [33], [36]. This involved specifying the gantry components' dimensions, shape, and spatial arrangement, including the toroidal magnet, superconducting coils, vector magnet, and patient interface.

In FLUKA, the geometric is constructed using a combination of bodies, zones, regions, and lattices (Figure 4.4).

Figure 4.4. FLUKA geometry construction of bodies, zones, regions, and lattice.

The geometric representation of GaToroid within FLUKA necessitates a meticulous approach. It is constructed from a complex integration of 131 distinct bodies. Each body is intricately linked to its corresponding region, resulting in a total of 32 regions. To further refine the geometry, 167 zones and 16 lattices are also incorporated. These intricate details are defined within the FLUKA input card, ensuring a comprehensive representation of GaToroid's structure. For a visual reference to the prototype model described in Section 4.1, refer to Figure 4.5, which serves as an illustrative guide.
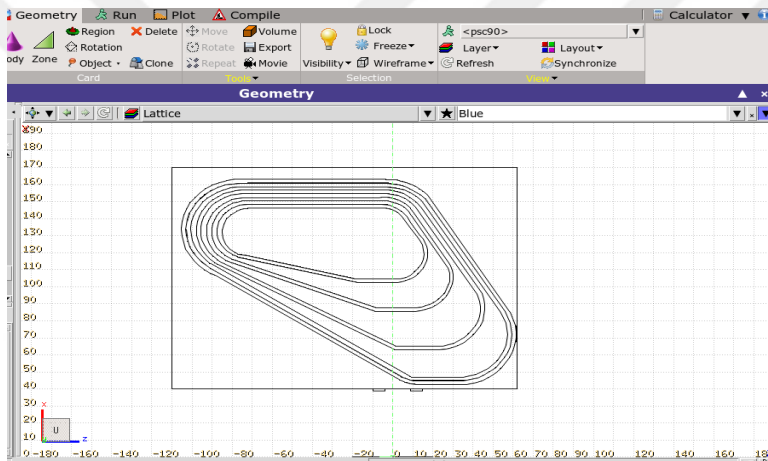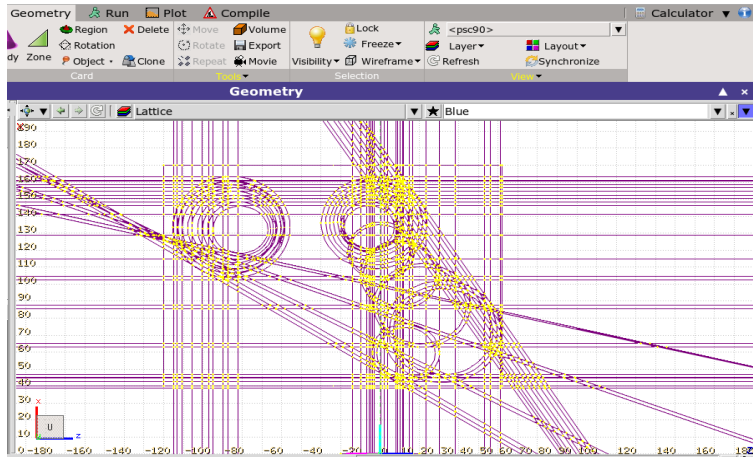
Figure 4.5. Prototype model illustration for GaToroid geometry.

To ensure accurate representation and facilitate visualization, the final structure of GaToroid is depicted in Figure 4.6. This multi-view figure showcases GaToroid's real dimensions and sizes from various angles. The dimensional details employed in this figure precisely reflect those provided in Table 4.2.
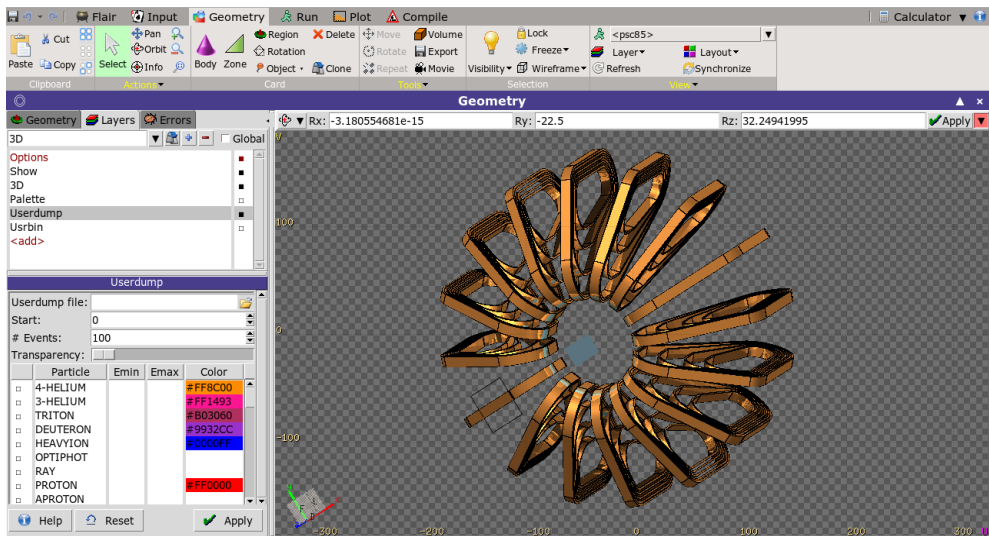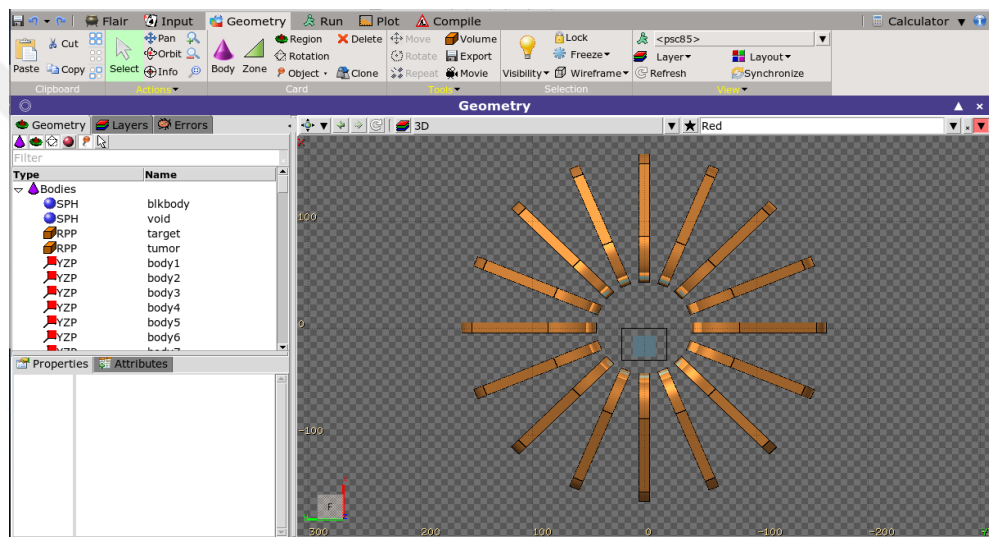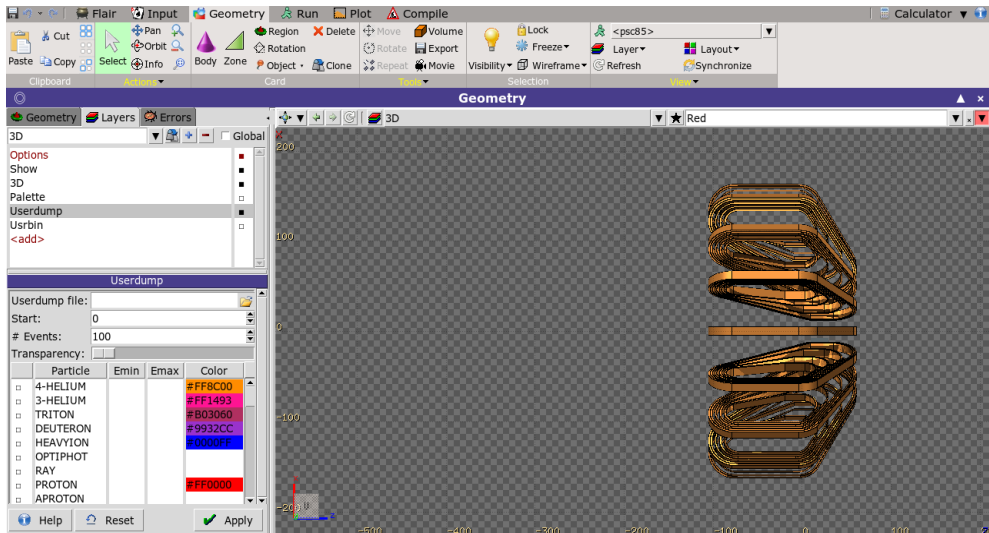
Figure 4.6. Final GaToroid geometry in side-view (top), front-view (middle), and rotated-view (bottom).

Within FLUKA, various materials can be assigned to distinct spatial regions within the simulation geometry. This includes the utilization of materials from its pre-defined database or user-defined compounds. In this study, the objective is to ensure the unobstructed passage of the proton beam through the space between consecutive coils (pancakes) toward the patient's body. To achieve this, a vacuum material is assigned to this intervening space. Consequently, the protons encounter no obstacles within this region and are solely subjected to the magnetic field generated by GaToroid. A water phantom represents the patient's body within the simulation.

4.2.3. Beam definition

The configuration of the proton beam source must be meticulously defined, including its energy, initial position, beam direction, and any collimation or shaping elements. Defining these source parameters is crucial for replicating the characteristics of the proton beam entering GaToroid in the simulation. In FLUKA, there are two different methods to implement the beam: BEAM card and SOURCE card.

4.2.3.1. BEAM card

FLUKA utilizes the BEAM card to define the characteristics of the primary particle beam. This card facilitates the specification of various parameters, including particle type, energy/momentum, and divergence. Additionally, the BEAMPOS card defines the starting position and direction of the beam source. Users can easily set up a monoenergetic proton beam using these two cards by directly inputting the desired energy value and other relevant properties.

4.2.3.2. SOURCE card

The SOURCE card provides a more flexible way to define the primary particle source, allowing for complex customizations. Users can activate a user-defined source routine with the SOURCE card in the FLUKA input file. This method is particularly useful for simulations requiring intricate beam properties or spatial distributions that are not straightforward to define using the BEAM card alone.

This capability is particularly valuable for simulations where the interaction of multiple distinct particle sources needs to be investigated. The user-defined routine can be programmed to generate each source with its own characteristics, allowing for a more comprehensive analysis of complex scenarios.

4.2.4. Magnetic field

For applying the magnetic field in FLUKA, there are two main approaches: using the 'MGNFIELD' card directly in the input file or activating a user routine through `magfld.f` file.

The availability of user routines within FLUKA empowers researchers with the capability for complete customization in managing the transport of charged particles within any user-defined magnetic field configuration. This feature proves particularly valuable when simulating GaToroid due to the inherent complexity of its magnetic field. To achieve an accurate representation of this intricate magnetic field within the FLUKA simulation, a user-defined routine becomes necessary.

This process entails the creation of a custom user routine specifically designed to define the magnetic field based on previously obtained multipole expansions. The multifaceted nature of GaToroid's magnetic field necessitates a detailed and precise implementation. Predefined field options available within FLUKA are simply inadequate to capture the nuances of this complex field. Here, the flexibility offered by user routines in FLUKA becomes crucial.

By incorporating the multipole expansions into the `magfld.f` routine, the magnetic field can be meticulously modeled, ensuring an accurate representation within the simulation. This precise approach is essential for reliable simulation of GaToroid's effects on the proton beam.

5. RESULTS AND DISCUSSION

5.1. Introduction

This chapter focuses on calculating the magnetic field within the GaToroid structure. The methodology established in the previous chapter is the foundation for this analysis. A comprehensive examination of the magnetic field distribution and its characteristics throughout the GaToroid will be undertaken. Next, this calculated magnetic field is applied within the FLUKA simulation framework to investigate the dynamic properties of the system.

This includes an in-depth examination of the interactions between the magnetic field and the proton beam, assessing how GaToroid influences the trajectory, stability, and overall behavior of the proton beam during therapy.

Following this, the performance and efficacy of GaToroid evaluated by analyzing its impact on the proton beam's delivery and targeting precision. This analysis will be crucial for understanding how GaToroid can be optimized for better control and accuracy in proton therapy.

Finally, FLUKA simulation results will be used to calculate several critical parameters essential for effective proton therapy, such as dose distribution, energy deposition, LET, and treatment accuracy. These parameters will be meticulously analyzed to gain valuable insights into the potential improvements and clinical benefits of incorporating GaToroid in proton therapy systems.

5.2. Calculation of the Magnetic Field for GaToroid

This section presents our comprehensive analysis of the magnetic field distribution within GaToroid. This analysis provides insights into the magnetic field's spatial characteristics, strength, and uniformity, critical for effectively manipulating proton beams in therapy.

The magnetic field components B_ξ, B_η, and B_ϕ in GaToroid toroidal coordinates, were computed using the multipolar expansion method, with the coefficients determined

through the fitting procedures discussed in the previous chapter. These components will be evaluated at various points of regions within GaToroid, providing a detailed map of the magnetic field.

The first step in evaluating the magnetic field involves calculating the scalar field for a portion of the toroid. This calculation is performed on a grid selected within GaToroid, composed of 16 coils. This portion, optimized as described in [46], is selected for the poloidal angle $0 < \phi < \pi/4$, with the following properties:

Toroidal index: n = 1, 16, 32.

Poloidal index: m = 1, 2, 3.

Current of each pancake: 1 kA.
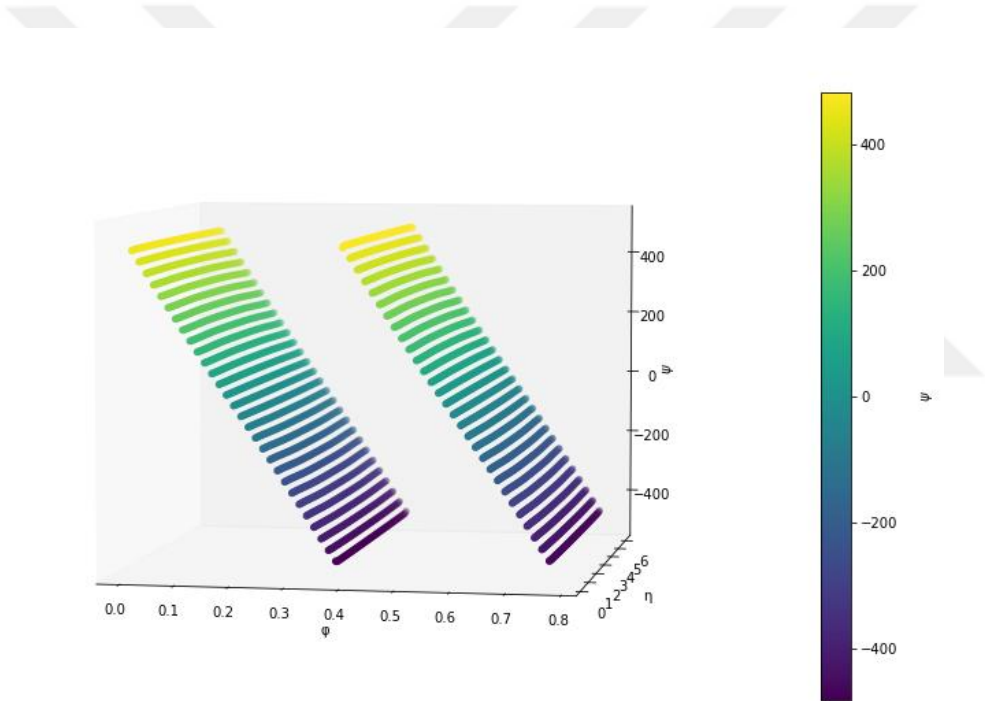
Figure 5.1. Scalar field 0<ϕ<π/4.

Following determining the scalar field for $L = S = 60$ [55], the fitting method outlined in Chapter 3 is employed to establish the value of M_{00}^{ϕ}. This stage facilitates the identification of the optimal value of M_{00}^{ϕ} that achieves minimal root mean square error and maximizes the R^2 value (Section 3.3.3.1).

Figure 5.2 shows the relationship between the selection of poloidal angle ϕ and the resulting value of M_{00}^{ϕ}. As mentioned in Section.3.3.3, ϕ can be chosen from S

equidistant values (here $\phi_s = \frac{(\pi/4-0)s}{S-1}$, with $s = 0, 1, 2, ...S\text{-}1$). To gain insights into how M_{00}^{ϕ} behaves under these varying conditions, three specific cases (A, B, and C) are selected for comparative analysis.

(A) $\phi = 0.5857$
     $R^2 = 0.9999$
     RMSE $= 0.0011$

(B) $\phi = 0.5325$
     $R^2 = 0.9999$
     RMSE $= 0.0185$

(C) $\phi = 0.4127$
     $R^2 = 0.9577$
     RMSE $= 0.2057$

Figure 5.2. RMSE and R^2 in different $\phi \subset (0,\pi/4]$.

- **Case A (Low RMSE, High R^2):**

  This case represents a scenario where the fitted curve closely aligns with the data points, reflected in a low RMSE and a high R^2 value. Here, ϕ is chosen to be 0.5857 (one of the 60 available options). This particular selection of ϕ contributes to the strong fit observed in Case A, leading to $M_{00}^{\phi} = 14.2077$.

- **Case B (Low RMSE, High R^2):**

  Similar to Case A, Case B exhibits a low RMSE and a high R^2, indicating a good fit. However, ϕ in this case is chosen to be 0.5325, which differs slightly from Case A. Despite this variation in ϕ, Case B still yields a good fit, resulting in an $M_{00}^{\phi} = 266.2869$.

- **Case C (High RMSE, Low R^2):**
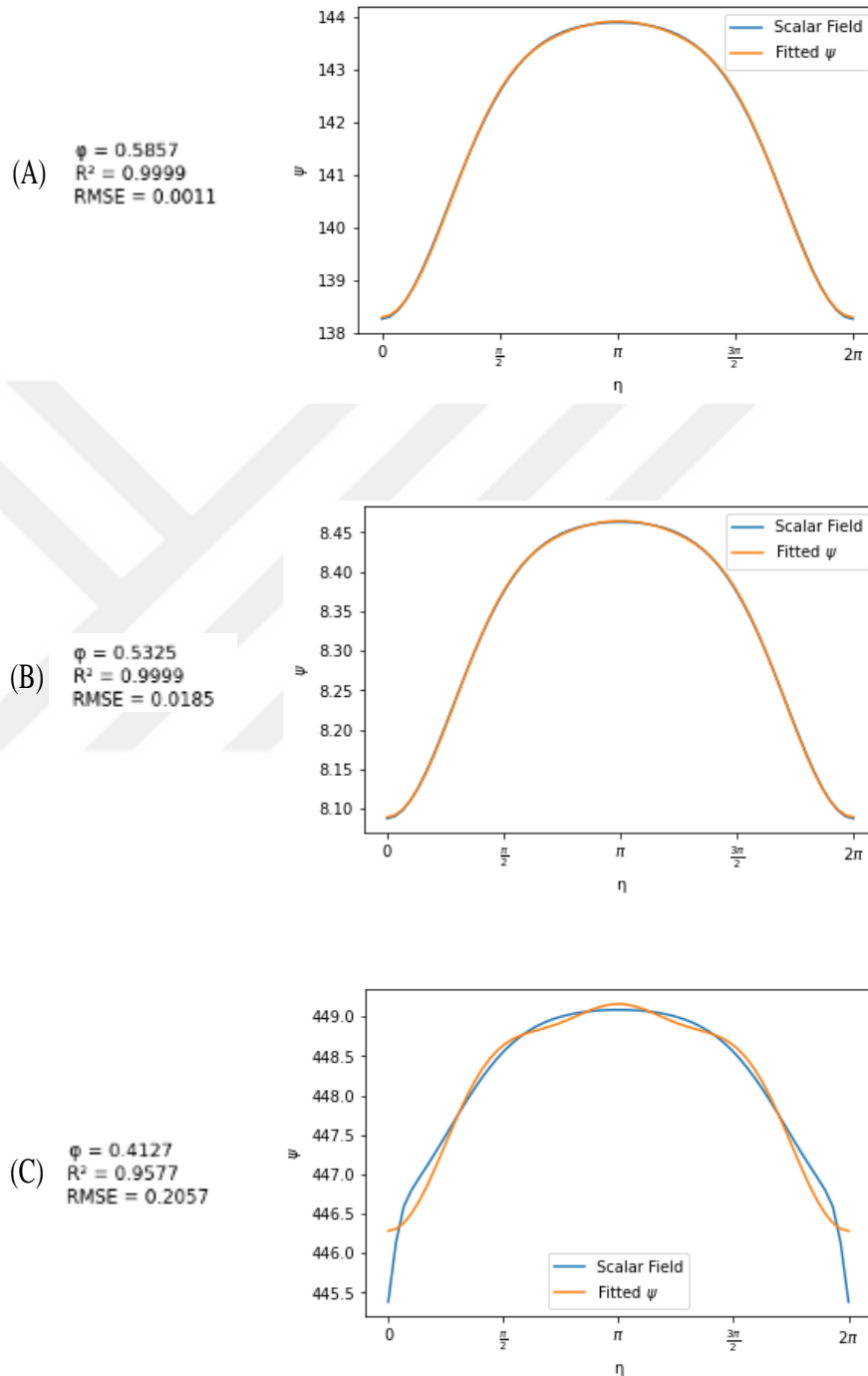
  In contrast to Cases A and B, Case C demonstrates a significantly poorer fit, evident from the high RMSE and low R^2. Here, ϕ is selected as 0.4127. This particular choice of ϕ leads to a substantial mismatch between the fitted curve and the data, resulting in a less trustworthy $M_{00}^{\phi} = 1085.9539$. The significant deviations observed in Case C highlight that this selection of ϕ may not be suitable for capturing the underlying physical phenomenon.

By analyzing these three cases, valuable insights were gained into how the selection of ϕ from the S choices can influence the M_{00}^{ϕ} value. Cases A and B showcase the importance of goodness-of-fit metrics in selecting reliable M_{00}^{ϕ} values. Case C serves as a cautionary tale, emphasizing the need to carefully consider ϕ selection to ensure an accurate representation of the physical process.

While evaluating all 60 possible ϕ values for inclusion here may not be feasible, case A demonstrates the optimal fit based on the combined metrics of minimum RMSE and maximum R^2. Therefore, the corresponding value of $M_{00}^{\phi} = 14.2077$ was chosen with confidence and adapted for subsequent calculations involving the determination of the multipole constants. This value will be retained as a fixed parameter in our ongoing work.

Once the value of M_{00}^{ϕ} is determined, the next step is substituting it into equation 3.8. Following the detailed fitting procedure, this approach will yield the desired multipolar components for the toroid with its specific configuration of 16 individual windings, as presented in Table 5.1.

Table 5.1. Multipolar moments of GaToroid system.

m	n	Mcc	Mcs	Msc	Mss
1	0	0.96319	0	-7.11E-07	0
1	16	0	-1.97E-13	0	0
1	32	0	0	0	0
2	0	-2.3194	0	-3.83E-05	0
2	16	0	0	0	0
2	32	0	0	0	0
3	0	-16.3411	0	4.06E-04	0
3	16	0	0	0	0
3	32	0	0	0	0

5.3. Magnetic Field Distribution

Equations 3.14 express the magnetic field distribution in toroidal coordinates by incorporating multipole coefficients of Table 5.1.

The magnetic field components are converted to Cartesian coordinates (as detailed in Section 3.4) and subsequently entered into the `magfld.f` FORTRAN file. With the initial conditions and a predetermined current value in the coils established, FLUKA is then executed. The observed distribution of the magnetic field aligns with previously predicted behavior [36].
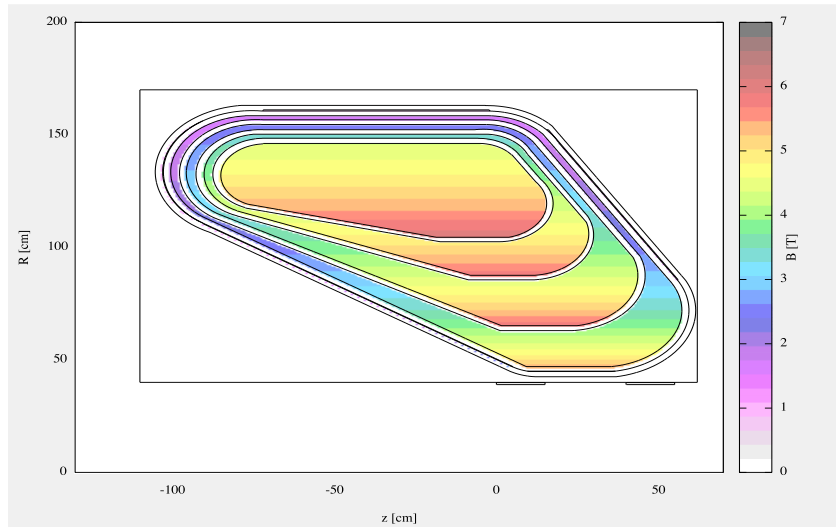
Figure 5.3. Distribution of magnetic field intensity in GaToroid.

Figure 5.3 presents a two-dimensional cross-sectional representation of the magnetic field distribution within GaToroid's interior space. As can be observed, the magnetic field exhibits a non-uniform distribution. Notably, the field intensity reaches a maximum of 7 T in specific regions while exhibiting a gradual decrease in others.

It is worth noting that an ideal toroidal field distribution would exhibit a decrease in intensity proportional to $1/R$ as the distance from the z-axis increases (due to Biot-savart rule). However, Figure 5.3 clearly demonstrates that the GaToroid's, specifically its grading, compensates for this inherent decrease. This observation suggests that GaToroid's design modifies the field distribution to achieve a more desirable profile within its operational volume.

5.4. Proton Beam Deflection

Protons, the positively charged constituents of atomic nuclei, interact with magnetic fields through a force known as the Lorentz force. This force deflects protons from their initial trajectory, causing them to follow a curved path. The magnitude and direction of this curvature are dictated by the strength and orientation of the magnetic field, as well as the velocity of the protons.

5.4.1. Interaction with GaToroid magnetic field

To understand GaToroid's functionality, an initial determination of the optimal magnetic field configuration within its structure is undertaken. Once established, the

66

behavior of a proton beam traversing GaToroid can be simulated using FLUKA. The beam's characteristics, including energy and direction, are defined in Table 5.2.

Table 5.2. Proton beam characteristics for FLUKA simulation.

Parameter	value	Unit
Energy	220	MeV
Source Location	-3.6	m
Entrance Angle (α)	18.69°	deg

FLUKA simulations facilitate the visualization of the interaction between the proton beam and GaToroid's magnetic field. As illustrated in Figure 5.4, when the beam traverses the empty space within the toroidal structure (while irradiated in the x-z plane), it experiences a significant deflection towards the isocenter.
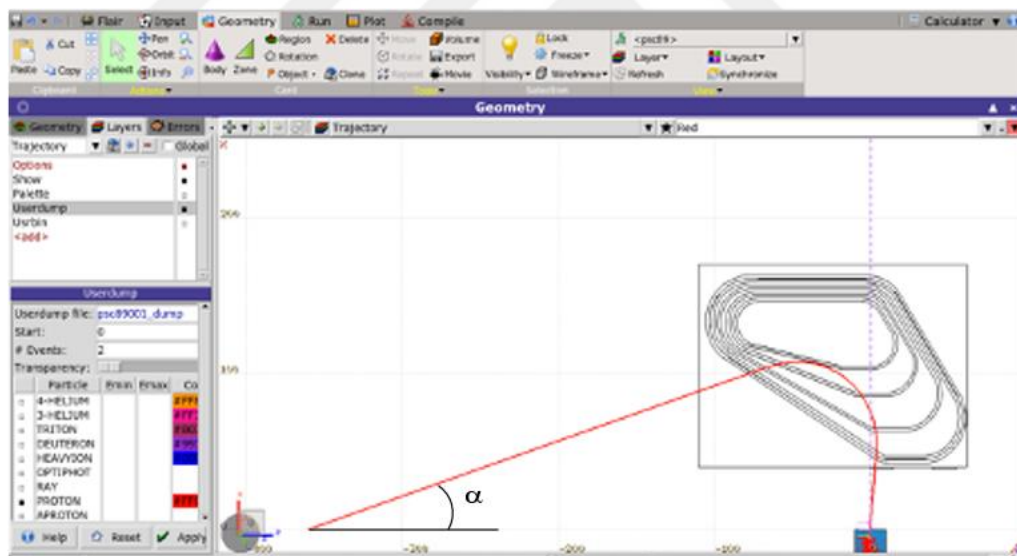
Figure 5.4. The tracking of proton beams with E = 220 MeV impinging GaToroid.

The beam is initially directed with a specific entrance angle (α) towards the void between adjacent coils. Upon reaching this inter-coil region, the pre-existing magnetic field exerts magnetic forces, inducing a deflection from the initial path and guiding the beam towards the isocenter point. It is important to note that any variations in the initial beam parameters, such as launch energy or angle, directly influence the final beam position. This dependence on launch conditions allows for precise control over the

depth and spatial distribution of the dose delivered to the target tumor within the patient.

5.4.2. Directional control

A key advantage of GaToroid's lies in its ability to manipulate the direction of this deflection. By meticulously adjusting the launch angle of the proton beam, deflection can be achieved in any of the empty spaces between the 16 coils constituting the device. This maneuverability is the core functionality of GaToroid. GaToroid essentially empowers medical professionals to precisely steer the proton beam towards the tumor from various directions. This eliminates the need for patient repositioning or gantry movement during treatment. This directional control facilitates a more targeted approach to cancer therapy, potentially minimizing damage to healthy tissues surrounding the tumor.

5.4.3. Determination of launch angles for isocenter targeting

This section outlines a method for obtaining the appropriate launch angles required for proton beams of varying energies to reach the isocenter. An iterative approach is employed, where beams with specific energies are directed towards the GaToroid model.

The USERDUMP card within the input cards of FLUKA is utilized to track the beam trajectory. The corresponding energy and launch angle are recorded if the final beam position coincides with the isocenter. While this method can be time-consuming, it offers high accuracy (range 0.1 mm) in determining the necessary parameters for effective treatment planning, as evidenced by the results presented in Table 5.3. Notably, this approach is applicable for targeting tumors located at various depths within the patient's body, encompassing both superficial and deep-seated lesions.

Table 5.3. Energy and launch angles.

Beam	Energy [MeV]	α^o (accuracy 0.1 mm)	α^o (accuracy 10 mm)
E1	70	14.57	14.69
E2	100	15.46	15.58
E3	130	17.43	17.40
E4	160	17.74	17.62
E5	190	18.17	18.06
E6	220	18.69	18.69
E7	250	20.38	20.32

Figure 5.5 provides an illustration depicting all proton beams and their corresponding launch angles with corresponding energies. This representation visually demonstrates the convergence of all beams at the isocenter. This visualization is achievable for various azimuthal angle configurations, highlighting the inherent capability of GaToroid system for beam steering.
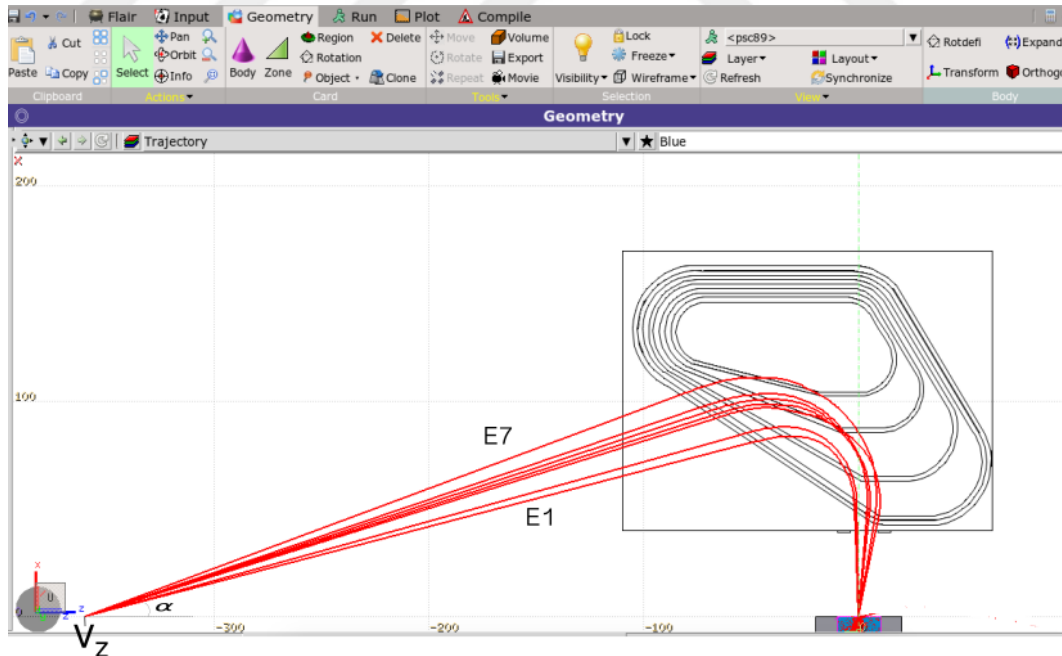

Figure 5.5. Tracking proton beams of varying energy and angle impinging on GaToroid (Table 5.3.)

Beyond the well-defined treatment parameters (Table 5.3), even slight adjustments to the proton beam's energy or incident angle can demonstrably alter its trajectory. This

phenomenon, a consequence of the Lorentz force exerted by the magnetic field (Figures 5.6 and 5.7), highlights the crucial role of precise magnet control. Therefore, a highly sensitive vector magnet is essential, and its placement and orientation must be meticulously calibrated to accommodate variations in beam energy.

This level of control unlocks a powerful therapeutic strategy. By strategically manipulating the beam exit angle from the vector magnet, the entire tumor region can be scanned with a precisely tailored energy distribution. This comprehensive approach to irradiation holds immense potential for enhancing treatment efficacy. Additionally, it offers the benefit of minimizing both radiation time and the unnecessary exposure of healthy tissue to additional dose.
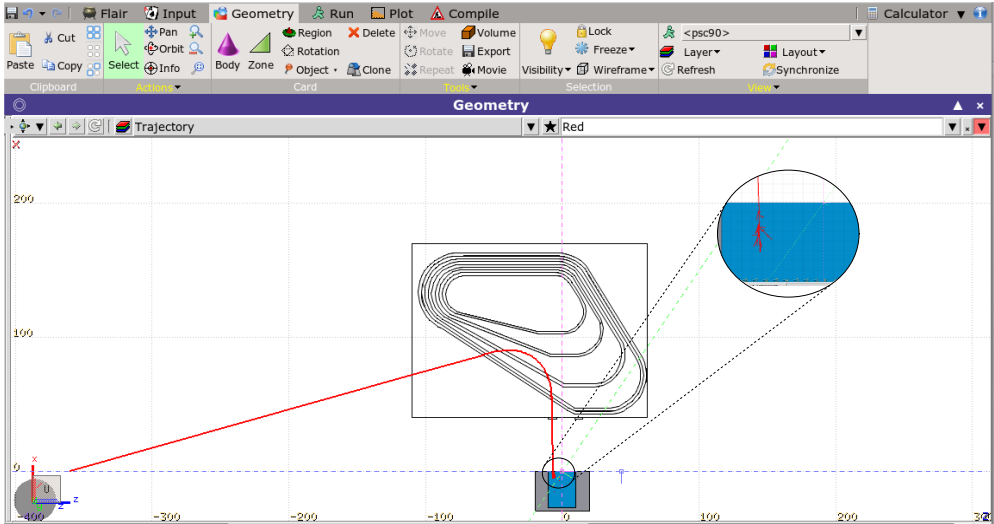

Figure 5.6. The beam energy is 70 MeV and $\alpha = 16°$.
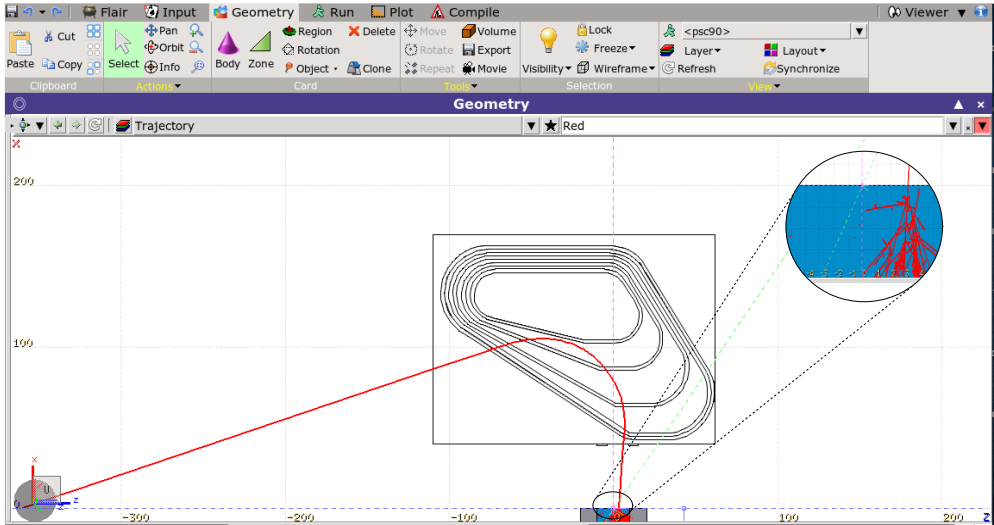
Figure 5.7. The beam energy is 250 MeV and $\alpha = 19°$.

Furthermore, GaToroid design facilitates access to tumors positioned at diverse angular orientations within the patient, eliminating the need for patient or gantry repositioning during treatment. This eliminates the requirement for heavy component rotations, allowing for a simplified and potentially more efficient treatment workflow (Figure 5.8).

Figure 5.8. GaToroid facilitates diverse beam angulations without repositioning. side-view (top), and front-view (bottom).

5.5. Evaluation of GaToroid's Performance

The physical characteristics of charged particles, including protons, significantly influence their biological effects during irradiation. The inverted dose–depth profile of charged particles allows for more precise targeting, improving volume conformity in

tumor treatments when compared to photons. This precision minimizes damage to surrounding healthy tissues. Additionally, it offers an enhanced RBE in t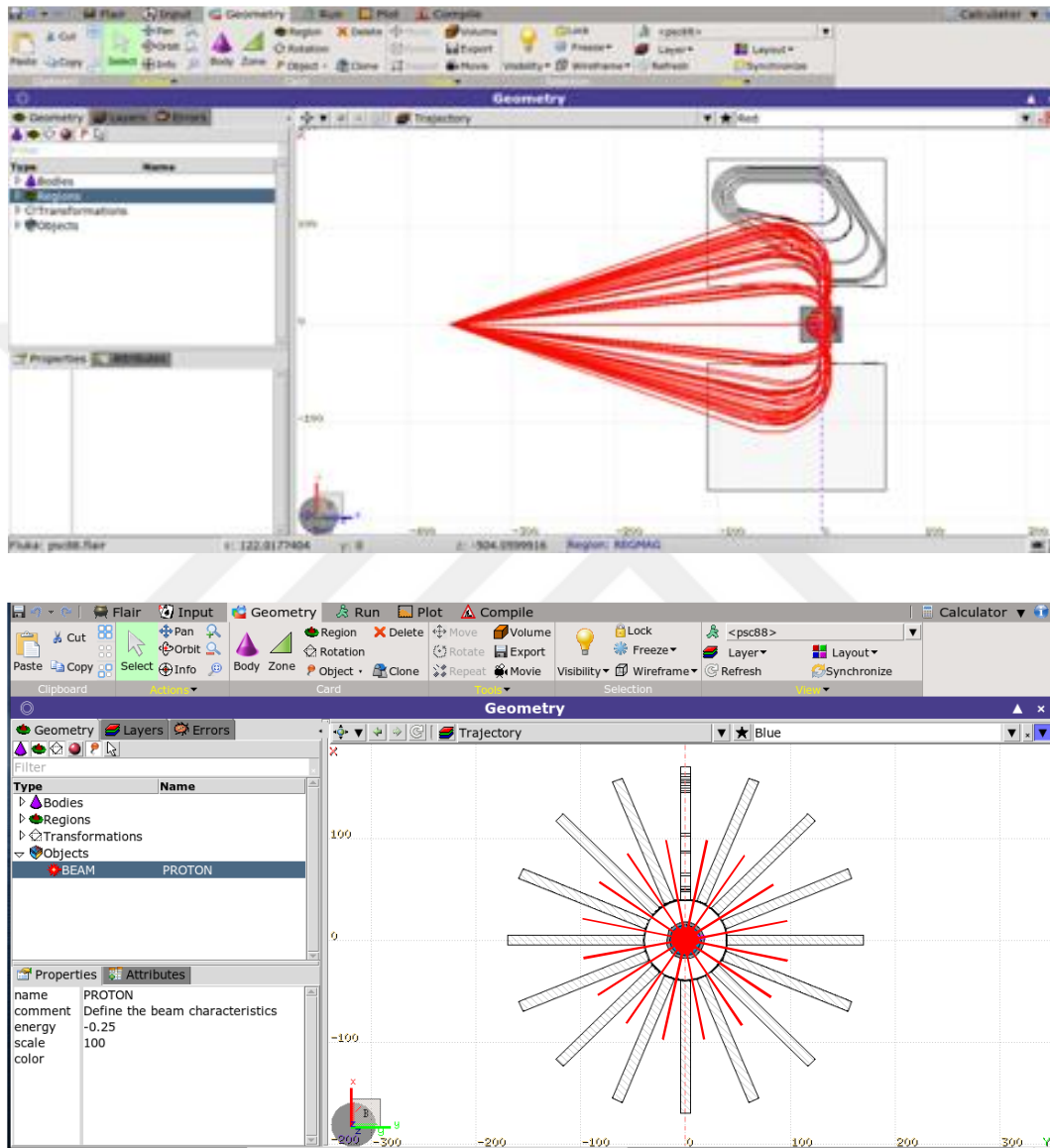he tumor region, further increasing the efficacy of the treatment. This combination of dose distribution and biological effectiveness makes charged particle therapy a powerful tool in cancer treatment.

This section evaluates the performance of GaToroid in simulating the interaction between a proton beam and patient tissue. A water phantom is employed to replicate human body tissue, as it provides an accurate and standardized medium for comparison in medical simulations [56]. Three commonly used proton beam energies, typically available in medical centers, are selected for the study. The characteristics of the proton beams, including their energies, launch angles, and divergences, are detailed in Table 5.4. The simulation involves a total of 10^5 primary particles distributed across 5 cycles to ensure statistical reliability and a comprehensive analysis of the beam's behavior and its interaction with the target.

Table 5.4. Proton beam characteristics for different energies.

Energy (MeV)	79.7	146.9	201.0
Source Location (m)	-3.6	-3.6	-3.6
Launch Angle (α)	14.85	17.58	18.34
Divergence (mm rad)	1	1	1

5.5.1. Dose distribution

MC simulations have long been the standard for validating dose calculation algorithms in clinical radiation therapy [57]. This approach uses statistical methods to model radiation particle transport through tissues, considering complex interactions and anatomical variations. Integrating GaToroid within the FLUKA framework enables the assessment of changes in radiation dose distribution. This assessment can be carried out using various methods, such as scoring cards and advanced biasing techniques related to stopping power and mean-free path calculations.
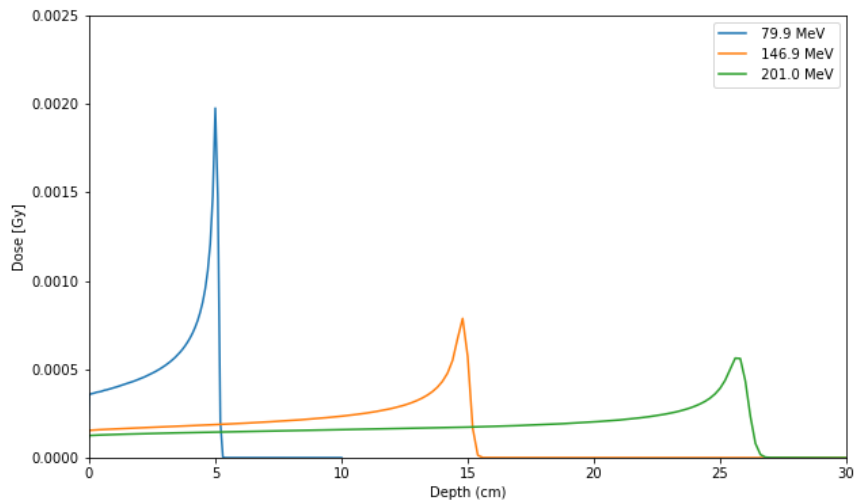
Figure 5.9. The distribution of dose for three different proton beams in table 5.4.

The dose distribution in the water phantom was measured for GaToroid system at three different energies. As illustrated in Figure 5.9, the dose received at 79.9 MeV is more than double the dose values observed for the other two energies. As expected, higher energies exhibit reduced interactions with tissues, resulting in a lower dose at different depths.

5.5.2. LET_t and LET_d

Using the procedure outlined in the Sections.1.9.1 and 1.9.2, the distributions of LET_t and LET_d as a function of depth were calculated for three different energies.

The results were obtained by considering the proton beams with the characteristics listed in Table 5.4, using FLUKA for the GaToroid system, and are consistent with the findings of [8]. As shown in Figures 5.10 and 5.11, different energies produce varying LET_t and LET_d values. Furthermore, it is possible to predict the outcomes of different energies to optimize treatment with a proton beam.
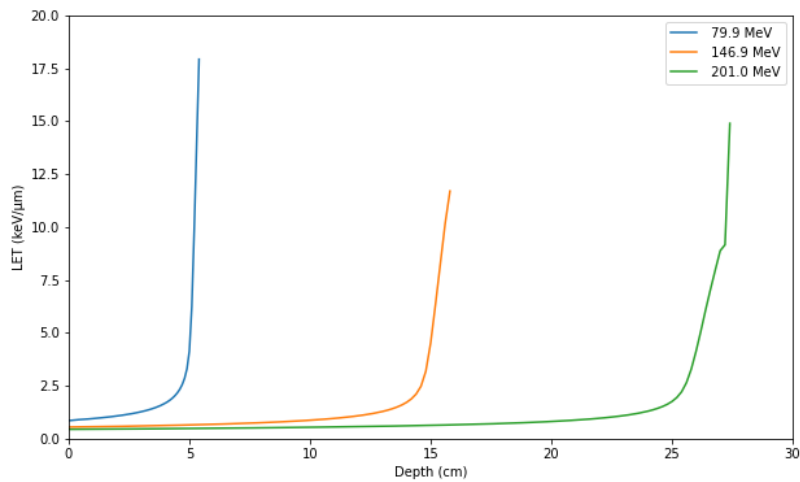
Figure 5.10. Distributions of LET_t for proton beams given in Table 5.4.
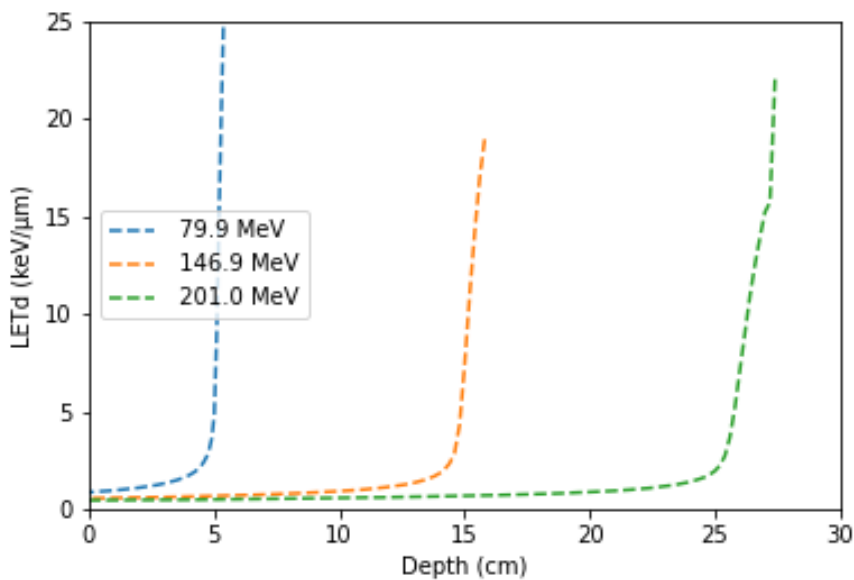
Figure 5.11. Distributions of LET_d for proton beams given in Table 5.4.

5.5.3. Energy deposition

The energy deposited in the medium by all proton beams listed in Table 5.4 can be determined through the interaction of protons with the water phantom, which follows the characteristic behavior of the Bragg peak -the point at which protons release the maximum energy just before coming to rest. Accordingly, Figure 5.12 illustrates the Bragg peak, showing the energy deposition as a function of the proton range in water for the relevant proton beams.
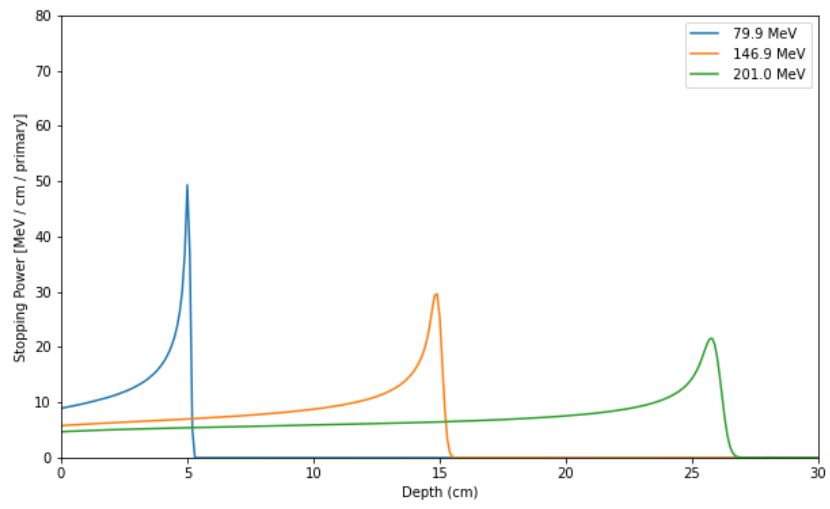
Figure 5.12. Energy deposited in the medium for different proton beams listed in Table 5.4.

6. CONCLUSION AND RECOMMENDATIONS

In this work, the magnetic field inside a novel toroidal gantry, called GaToroid, designed for proton therapy has been calculated using the multipolar moments. The obtained variable magnetic field has been embedded inside the simulated GaToroid region and proton beams with different energies between 70-250 MeV have been sent at different angles with the GaToroid axis, whose center resides the patient body. The protons with energies in the range given above are expected to reach the target volume thanks to the magnetic field inside GaToroid.

The FLUKA simulations have demonstrated that the calculated magnetic field can effectively deflect and steer the proton beams with different energies to the isocenter where the target, the tumor, is located. This can be achieved if the incident (zenith) angle of the beam is properly set. The appropriate angles for each proton energy have been selected from the output of simulations. Having determined these angles, it is then possible to repeat the procedure to bombard the target region from different azimuthal directions in order to have a three-dimensional scanning thanks to the symmetric structure of GaToroid. The directional control capability can improve targeting accuracy and conformality of the dose distribution within the patient.

The simulations have also showed promise for achieving favorable LET profiles within the target volume, consistent with the results in the literature.

Overall, the findings suggest that the toroidal gantry design holds significant promise for advancements in proton therapy. The GaToroid's ability to manipulate the beam path offers several potential benefits, including improved targeting precision, reduced dose to healthy tissues, and potentially enhanced biological effects of the treatment.

However, further research is necessary to fully realize the clinical potential of the GaToroid technology. Future work should focus on optimizing the magnetic field configuration for improved beam control. In vitro and in vivo experiments are crucial for validating the simulated results and assessing the biological efficacy of the GaToroid design. Ultimately, clinical trials will be needed to demonstrate the safety and effectiveness of this novel approach in cancer treatment.

This dissertation has laid a strong foundation for developing toroidal gantry technology in proton therapy. With continued research and refinement, GaToroid can revolutionize the field of cancer treatment by offering a more precise, targeted, and potentially more effective approach for patients.

REFERENCE

[1]   L. Harkness-Brennan, *An Introduction to the Physics of Nuclear Medicine:* Morgan & Claypool Publishers, 2018. doi: 10.1088/978-1-6432-7034-0.

[2]   N. Tsoulfanidis and S. Landsberger, *MEASUREMENT & DETECTION of RADIATION*, 4th Edition. 2014.

[3]   H. Murshed, "Radiation Physics, Dosimetry, and Treatment Planning," in *Fundamentals of Radiation Oncology*, Elsevier, 2019, pp. 3–37. doi: 10.1016/B978-0-12-814128-1.00001-5.

[4]   T. D. Malouff and D. M. Trifiletti, "Principles and Practice of Particle Therapy".

[5]   F. H. Attix, *Introduction to radiological physics and radiation dosimetry*. New York: Wiley, 1986.

[6]   E. W. Collings, L. Lu, N. Gupta, and M. D. Sumption, "Accelerators, Gantries, Magnets and Imaging Systems for Particle Beam Therapy: Recent Status and Prospects for Improvement," *Front. Oncol.*, vol. 11, p. 737837, Feb. 2022, doi: 10.3389/fonc.2021.737837.

[7]   H. Suit *et al.*, "Proton vs carbon ion beams in the definitive radiation treatment of cancer patients," *Radiotherapy and Oncology*, vol. 95, no. 1, pp. 3–22, 2010, doi: https://doi.org/10.1016/j.radonc.2010.01.015.

[8]   F. Guan *et al.*, "Analysis of the track- and dose-averaged LET and LET spectra in proton therapy using the GEANT 4 Monte Carlo code," *Medical Physics*, vol. 42, no. 11, pp. 6234–6247, Nov. 2015, doi: 10.1118/1.4932217.

[9]   A. Helm and C. Fournier, "High-LET charged particles: radiobiology and application for new approaches in radiotherapy," *Strahlenther Onkol*, vol. 199, no. 12, pp. 1225–1241, Dec. 2023, doi: 10.1007/s00066-023-02158-7.

[10]   R. Mohan and D. Grosshans, "Proton therapy – Present and future," *Advanced Drug Delivery Reviews*, vol. 109, pp. 26–44, Jan. 2017, doi: 10.1016/j.addr.2016.11.006.

[11]   H. K. Byun *et al.*, "Physical and Biological Characteristics of Particle Therapy for Oncologists," *Cancer Res Treat*, vol. 53, no. 3, pp. 611–620, Jul. 2021, doi: 10.4143/crt.2021.066.

[12]   R. Sandro, "Hadron Therapy Achievements and Challenges: The CNAO Experience," p. 229, 2022, doi: 10.3390/physics4010017.

[13]   R. Appleby, G. Burt, J. Clarke, and H. Owen, *The Science and Technology of Particle Accelerators*, 1st ed. Boca Raton: CRC Press, 2020. doi: 10.1201/9781351007962.

[14]   J. M. Park, J. Kim, and H.-G. Wu, "Technological Advances in Charged-Particle Therapy," *Cancer Res Treat*, vol. 53, no. 3, pp. 635–640, Jul. 2021, doi: 10.4143/crt.2021.706.

[15]   S. V. Bulanov *et al.*, "Laser ion acceleration for hadron therapy," 2014.

[16]   R. W. Garnett and R. L. Sheffield, "Overview of Accelerator Applications in Energy," *Rev. Accl. Sci. Tech.*, vol. 08, pp. 1–25, Jan. 2015, doi: 10.1142/S1793626815300017.

[17]   A. Degiovanni and U. Amaldi, "History of hadron therapy accelerators," *Physica Medica*, vol. 31, no. 4, pp. 322–332, Jun. 2015, doi: 10.1016/j.ejmp.2015.03.002.

[18]   E. Benedetto and M. Vretenar, "Innovations in the Next Generation Medical Accelerators for Therapy with Ion Beams," *J. Phys.: Conf. Ser.*, vol. 2687, no. 9, p. 092003, Jan. 2024, doi: 10.1088/1742-6596/2687/9/092003.

[19]   U. Amaldi *et al.*, "Accelerators for hadrontherapy: From Lawrence cyclotrons to linacs," *Nuclear Instruments and Methods in Physics Research Section A: Accelerators, Spectrometers, Detectors and Associated Equipment*, vol. 620, no. 2–3, pp. 563–577, Aug. 2010, doi: 10.1016/j.nima.2010.03.130.

[20]   J. Yap, A. De Franco, and S. Sheehy, "Future Developments in Charged Particle Therapy: Improving Beam Delivery for Efficiency and Efficacy," *Front. Oncol.*, vol. 11, p. 780025, Dec. 2021, doi: 10.3389/fonc.2021.780025.

[21]   M. T. F. Pivi, "The MedAustron particle therapy accelerator facility," *Health Technol.*, Apr. 2024, doi: 10.1007/s12553-024-00840-z.

[22]   E. Pearson, W. Kleeven, J. V. de Walle, and S. Zaremba, "THE NEW IBA SUPERCONDUCTING SYNCHROCYCLOTRON (S2C2): FROM MODELING TO REALITY".

[23]   B. Hidding *et al.*, "Progress in Hybrid Plasma Wakefield Acceleration," *Photonics*, vol. 10, no. 2, p. 99, Jan. 2023, doi: 10.3390/photonics10020099.

[24]   L. Rossi *et al.*, "A European Collaboration to Investigate Superconducting Magnets for Next Generation Heavy Ion Therapy," *IEEE Trans. Appl. Supercond.*, vol. 32, no. 4, pp. 1–7, Jun. 2022, doi: 10.1109/TASC.2022.3147433.

[25]   U. Ratzinger, B. Koubek, and H. HVoreeltteenramr, "Linac Design Within HITRIplus for Particle Therapy".

[26]   E. De Matteis *et al.*, "Conceptual Design of an HTS Canted Cosine Theta Dipole Magnet for Research and Hadron Therapy Accelerators," *IEEE Trans. Appl. Supercond.*, vol. 34, no. 5, pp. 1–5, Aug. 2024, doi: 10.1109/TASC.2024.3360210.

[27]   R. Tesse, A. Dubus, E. Gnacadja, C. Hernalsteens, N. Pauly, and S. et al Boogert, "Shields, seamless beam and radiation transport simulations of IBA proteus systems using BDSIM," in *Proceedings of the international computational accelerator physics conference (ICAP'18)*, 2018. [Online]. Available:
http://accelconf.web.cern.ch/AccelConf/icap2018/talks/supag11_talk.pdf.

[28]   C. Priano, P. Fabbricatore, S. Farinon, R. Musenich, M. Perrella, and S. Squarcia, "A superconducting magnet for a beam delivery system for carbon ion cancer therapy," *IEEE Transactions on Applied Superconductivity*, vol. 12, no. 1, pp. 988–992, 2002, doi: 10.1109/TASC.2002.1018566.

[29]   M. Prioli, S. Sorti, and L. Rossi, "Dissemination Level: Public Work Package: WP8 Lead Beneficiary: INFN".

[30]   Y. Iwata *et al.*, "Design of a superconducting rotating gantry for heavy-ion therapy," *Phys. Rev. ST Accel. Beams*, vol. 15, no. 4, p. 044701, Apr. 2012, doi: 10.1103/PhysRevSTAB.15.044701.

[31]   A. Godeke *et al.*, "Research at Varian on applied superconductivity for proton therapy," *Supercond. Sci. Technol.*, vol. 33, no. 6, p. 064001, Jun. 2020, doi: 10.1088/1361-6668/ab804a.

[32]   Y. Iwata *et al.*, "Recent progress of a superconducting rotating-gantry for carbon-ion radiotherapy," *Nuclear Instruments and Methods in Physics Research Section B: Beam Interactions with Materials and Atoms*, vol. 406, pp. 338–342, Sep. 2017, doi: 10.1016/j.nimb.2016.10.040.

[33]   L. Bottura, E. Felcini, G. De Rijk, and B. Dutoit, "GaToroid: A novel toroidal gantry for hadron therapy," *Nuclear Instruments and Methods in Physics Research Section A: Accelerators, Spectrometers, Detectors and Associated Equipment*, vol. 983, p. 164588, Dec. 2020, doi: 10.1016/j.nima.2020.164588.

[34]   E. Felcini, L. Bottura, J. Van Nugteren, G. De Rijk, G. Kirby, and B. Dutoit, "Magnetic Design of a Superconducting Toroidal Gantry for Hadron Therapy," *IEEE Trans. Appl. Supercond.*, vol. 30, no. 4, pp. 1–5, Jun. 2020, doi: 10.1109/TASC.2020.2966174.

[35]   L. Bromberg and M. Philip C, "Toroidal Bending Magnets for Hadron Therapy Gantries," *United States Patent*, 2017.

[36]   E. Felcini, "Analysis of a Novel Toroidal Configuration for Hadron Therapy Gantries".

[37]   C. Ahdida *et al.*, "New Capabilities of the FLUKA Multi-Purpose Code," *Front. Phys.*, vol. 9, p. 788253, Jan. 2022, doi: 10.3389/fphy.2021.788253.

[38]   R. S. Augusto *et al.*, "Experimental validation of the FLUKA Monte Carlo code for dose and β^+ -emitter predictions of radioactive ion beams," *Phys. Med. Biol.*, vol. 63, no. 21, p. 215014, Oct. 2018, doi: 10.1088/1361-6560/aae431.

[39]   A. Ferrari, P. R. Sala, A. Fasso, and J. Ranft, "a multi-particle transport code".

[40]   G. Battistoni *et al.*, "The FLUKA Code: An Accurate Simulation Tool for Particle Therapy," *Front. Oncol.*, vol. 6, May 2016, doi: 10.3389/fonc.2016.00116.

[41]   V. Andersen *et al.*, "The fluka code for space applications: recent developments," *Advances in Space Research*, vol. 34, no. 6, pp. 1302–1310, Jan. 2004, doi: 10.1016/j.asr.2003.03.045.

[42] M. Bektasoglu and M. Ali Mohammad, "Investigation of radiation shielding properties of TeO –ZnO–Nb O –Gd O glasses at medical diagnostic energies," *Ceramics International*, vol. 46, no. 10, pp. 16217–16223, Jul. 2020, doi: 10.1016/j.ceramint.2020.03.177.

[43] M. Ali Mohammad and M. Bektasoglu, "Comparative study of two bismuth–borate glasses in terms of gamma shielding parameters at medical diagnostic energies and neutron shielding characteristics," *Materials Chemistry and Physics*, vol. 255, p. 123609, Nov. 2020, doi: 10.1016/j.matchemphys.2020.123609.

[44] M. Bektasoglu and M. A. Mohammad, "Gamma and neutron shielding performance of some heavy metal-incorporated borate glasses," *Pramana - J Phys*, vol. 96, no. 2, p. 70, Jun. 2022, doi: 10.1007/s12043-022-02309-y.

[45] L. Gambini, M. Breschi, E. Felcini, A. Cristofolini, and L. Bottura, "An Algorithm for Toroidal Field Harmonics Computation in Arbitrary Magnetic Configurations," *IEEE Trans. Appl. Supercond.*, vol. 30, no. 4, pp. 1–5, Jun. 2020, doi: 10.1109/TASC.2020.2970907.

[46] L. Gambini, "Expansion of the magnetic flux density field in toroidal harmonics," Master Thesis, Bologna U., Bologna, Italy, 2018. [Online]. Available: CERN-THESIS-2018-040,

[47] B. Faugeras, "Tokamak Plasma Boundary Reconstruction Using Toroidal Harmonics and an Optimal Control Method," *Fusion Science and Technology*, vol. 69, no. 2, pp. 495–504, Apr. 2016, doi: 10.13182/FST15-171.

[48] A.B. Kuznetsov and S.V. Shchepetov, "Method of magnetic analysis for stellarator equilibria," *Nuclear Fusion*, vol. 37, no. 3, p. 371, Mar. 1997, doi: 10.1088/0029-5515/37/3/I07.

[49] P. Moon and D. E. Spencer, *Field Theory Handbook*. Berlin, Heidelberg: Springer Berlin Heidelberg, 1961. doi: 10.1007/978-3-642-53060-9.

[50] P. M. C. Morse and H. Feshbach, *Methods of Theoretical Physics*. Technology Press, 1946. [Online]. Available: https://books.google.com.tr/books?id=CSxWAAAAMAAJ

[51] J. V. Stewart, *Intermediate Electromagnetic Theory*. in G - Reference,Information and Interdisciplinary Subjects Series. World Scientific, 2001. [Online]. Available: https://books.google.com.tr/books?id=mwLI4nQ0thQC

[52] A. Van Oosterom and J. Strackee, "The Solid Angle of a Plane Triangle," *IEEE Trans. Biomed. Eng.*, vol. BME-30, no. 2, pp. 125–126, Feb. 1983, doi: 10.1109/TBME.1983.325207.

[53] T. Nguyen, B. M. Nguyen, and G. Nguyen, "Building Resource Auto-scaler with Functional-Link Neural Network and Adaptive Bacterial Foraging Optimization," in *Theory and Applications of Models of Computation*, vol. 11436, T. V. Gopal and J. Watada, Eds., in Lecture Notes in Computer Science, vol. 11436. , Cham: Springer International Publishing, 2019, pp. 501–517. doi: 10.1007/978-3-030-14812-6_31.

[54] V. Vlachoudis, "Flair: A powerful but user friendly graphical interface for FLUKA," presented at the Mathematics, Computational Methods & Reactor Physics (M&C 2009), Saragota Springs, New York, 2009.

[55] S. Russenschuck, *Field Computation for Accelerator Magnets: Analytical and Numerical Methods for Electromagnetic Design and Optimization*, 1st ed. Wiley, 2010. doi: 10.1002/9783527635467.

[56] M. Arjunan, S. Sekaran, B. Sarkar, and S. Manikandan, "A homogeneous water-equivalent anthropomorphic phantom for dosimetric verification of radiotherapy plans," *J Med Phys*, vol. 43, no. 2, p. 100, 2018, doi: 10.4103/jmp.JMP_123_17.

[57] P. Lysakovski *et al.*, "Development and benchmarking of the first fast Monte Carlo engine for helium ion beam dose calculation: MonteRay," *Medical Physics*, vol. 50, no. 4, pp. 2510–2524, Apr. 2023, doi: 10.1002/mp.16178.

CURRICULUM VITAE

Name Surname   : Mosleh Ali MOHAMMAD

EDUCATION:

- **Undergraduate** : 2007, Iran, Urmia, Universityof Urmia, Faculty of Science, Physics Department

- **Graduate**   : 2009, Iran, Kermanshah, University of Razi, Physics Department, Quantum Field Theory

PUBLICATIONS, PRESENTATIONS AND PATENTS ON THE THESIS:

- M. Bektasoglu and M. Ali Mohammad, "Investigation of radiation shielding properties of TeO_2–ZnO–Nb_2O_5–Gd_2O_3 glasses at medical diagnostic energies," *Ceramics International*, vol. 46, no. 10, pp. 16217–16223, Jul. 2020, doi: 10.1016/j.ceramint.2020.03.177.

- M. Ali Mohammad and M. Bektasoglu, "Comparative study of two bismuth–borate glasses in terms of gamma shielding parameters at medical diagnostic energies and neutron shielding characteristics," *Materials Chemistry and Physics*, vol. 255, p. 123609, Nov. 2020, doi: 10.1016/j.matchemphys.2020.123609.

- M. Bektasoglu and M. A. Mohammad, "Gamma and neutron shielding performance of some heavy metal-incorporated borate glasses," *Pramana - J Phys*, vol. 96, no. 2, p. 70, Jun. 2022, doi: 10.1007/s12043-022-02309-y.

- M. Bektasoglu, I. Karnik, and M. A. Mohammad, "Investigation of gamma shielding parameters of some silica borotellurite glasses with different amounts of Bi_2O_3 at energies between 10 and 150 keV," *Radiation Physics and Chemistry*, vol. 207, p. 110855, Jun. 2023, doi: 10.1016/j.radphyschem.2023.110855.